J. Fluid Mech. (2023), *vol*. 977, A37, doi:10.1017/jfm.2023.679

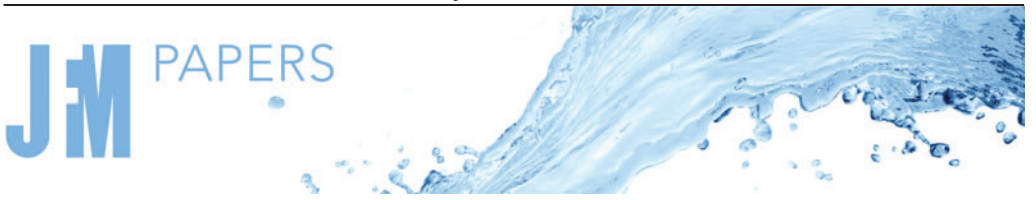

A data-driven method for modelling dissipation rates in stratified turbulence

Samuel F. Lewin[1], Stephen M. de Bruyn Kops[2], Colm-cille P. Caulfield[1,3,†] and Gavin D. Portwood[4]

[1]DAMTP, Centre for Mathematical Sciences, Wilberforce Road, Cambridge CB3 0WA, UK

[2]Department of Mechanical and Industrial Engineering, University of Massachusetts Amherst, Amherst, MA 01003, USA

[3]Institute for Energy and Environmental Flows, University of Cambridge, Madingley Road, Cambridge CB3 0EZ, UK

[4]Lawrence Livermore National Laboratory, Livermore, CA 94550, USA

(Received 27 January 2023; revised 13 June 2023; accepted 26 July 2023)

We present a deep probabilistic convolutional neural network (PCNN) model for predicting local values of small-scale mixing properties in stratified turbulent flows, namely the dissipation rates of turbulent kinetic energy and density variance, ε and χ. Inputs to the PCNN are vertical columns of velocity and density gradients, motivated by data typically available from microstructure profilers in the ocean. The architecture is designed to enable the model to capture several characteristic features of stratified turbulence, in particular the dependence of small-scale isotropy on the buoyancy Reynolds number $Re_b := \varepsilon/(\nu N^2)$, where ν is the kinematic viscosity and N is the background buoyancy frequency, the correlation between suitably locally averaged density gradients and turbulence intensity and the importance of capturing the tails of the probability distribution functions of values of dissipation. Empirically modified versions of commonly used isotropic models for ε and χ that depend only on vertical derivatives of density and velocity are proposed based on the asymptotic regimes $Re_b \ll 1$ and $Re_b \gg 1$, and serve as an instructive benchmark for comparison with the data-driven approach. When trained and tested on a simulation of stratified decaying turbulence which accesses a range of turbulent regimes (associated with differing values of Re_b), the PCNN outperforms assumptions of isotropy significantly as Re_b decreases, and additionally demonstrates improvements over the fitted empirical models. A differential sensitivity analysis of the PCNN facilitates a comparison with the theoretical models and provides a physical interpretation of the features enabling it to make improved predictions.

† Email address for correspondence: c.p.caulfield@damtp.cam.ac.uk

Key words: stratified turbulence, machine learning, turbulence modelling

1. Introduction

Turbulence is ubiquitous in the stably stratified ocean, where it facilitates the vertical mixing of water masses, thus playing a vital role in determining global transport of scalars such as heat, carbon and nutrients (Ivey, Winters & Koseff 2008; Talley *et al.* 2016). Observational estimates of small-scale turbulence quantities may be obtained using measurements of fluctuating density (or temperature, assuming a linear equation of state for a single dynamic scalar) and velocity fields captured by microstructure profilers, small probes that descend vertically through a column of water to depths of up to 6000 m and that have been deployed across much of the ocean (Waterhouse *et al.* 2014). The primary quantities of interest for diagnosing mixing rates are the rate of dissipation of density variance χ and the rate of dissipation of turbulent kinetic energy ε (defined below). Calculating precise values of ε and χ requires that nine spatial derivatives of velocities and three spatial derivatives of density be resolved simultaneously, and so in practice theoretical 'surrogate' models are commonly invoked which require only derivatives in a single coordinate direction (typically the vertical). Our focus here is on estimating ε and χ given exact values of these vertical derivatives alone as notionally measured by an idealised microstructure profiler. This facilitates a study of the underlying stratified turbulence dynamics and is a step toward improved mixing parameterisations 'output' from ocean measurement 'inputs', although it does not address other causes of uncertainty in obtaining accurate and robust *in situ* measurements of ε and χ, due for example to uncertainties in the mapping between the raw measurements and the vertical gradients of velocity and density (Gregg *et al.* 2018).

The majority of models for ε and χ are based on the fundamental assumption that turbulence is homogeneous and isotropic at small scales, although there have been efforts to model dissipation in stratified turbulence by use of a suitable proxy that captures the modifying influence of the stratification (Weinstock 1981; Fossum, Wingstedt & Reif 2013). We appeal to modern data-driven tools to supplement and extend existing theoretical models for ε and χ in the anisotropic stratified turbulent regime. Data-driven methods have become popular for the modelling of fluid flows due to their inherent ability to capture complex spatio-temporal dynamics (Salehipour & Peltier 2019; Brunton, Noack & Koumoutsakos 2020) and reveal insights into flow physics (Callaham *et al.* 2021; Couchman *et al.* 2021). They are also seeing widespread use for closure modelling, for example improving sub-grid parameterisation schemes in simulations of turbulence (Maulik *et al.* 2019; Portwood *et al.* 2021; Subel *et al.* 2021) and large-scale models of the atmosphere and ocean (Rasp, Pritchard & Gentine 2018; Bolton & Zanna 2019). Bayesian models that can provide uncertainty estimates as opposed to standard deterministic predictions are appealing in these settings as they give an important measure of model reliability and can accurately reproduce higher-order moments of a distribution of values over a set of data (Maulik *et al.* 2020; Barnes & Barnes 2021; Guillaumin & Zanna 2021).

Deep neural network models for determining the relationship between physical observables can be essentially described as the substitution of an equation whose functional form and accompanying parameters are based on known physical constraints for an equation whose functional form is determined by optimising an extremely large number of parameters using data obtained from measurements of the system: this results in what is commonly referred to as a 'black-box algorithm'. In cases where the underlying physical

processes are not fully understood, or not fully representable using a limited subset of system observables, these deep learning methods often result in greatly improved accuracy over traditional physics-based methods. This is, however, at the expense of generalisability to data from similar but distinct systems, where knowledge of how the underlying physics is encoded into a traditional theoretical model can be used to adapt it. Since they consist of such a large number of parameters – leaving the physics somewhat intractable – it is not obvious how to adapt deep learning models in the same way. To try to overcome this difficulty, either some information about the physics can be encoded into the architecture of the model *a priori* (such models are often referred to as 'physics-informed') (Ling, Kurzawski & Templeton 2016; Zanna & Bolton 2020; Beucler *et al.* 2021), or a highly general model can be analysed *a posteriori* to 'discover' physically relevant features (Toms, Barnes & Ebert-Uphoff 2020; Portwood *et al.* 2021).

Since exact observational measurements of ε and χ are not feasible at present for testing our methodology, we consider direct numerical simulations (DNS) of stably stratified turbulence (SST) as a model flow for the turbulence length and time scales of the ocean, the relevance of which is supported by a modest but increasing body of observations (Riley & Lindborg 2008). Broadly, such flows can be characterised by suitable Reynolds and Froude numbers, Re_h and Fr_h, as well as the Prandtl number Pr, defined here as

$$Re_h = \frac{U_h L_h}{\nu}, \quad Fr_h = \frac{U_h}{L_h N}, \quad Pr = \frac{\nu}{\kappa}. \tag{1.1a–c}$$

Here, U_h and L_h are horizontal velocity and length scales, N is a characteristic buoyancy frequency associated with the ambient stratification, ν is the kinematic viscosity and κ is the thermal diffusivity. The SST regime is then a turbulent flow regime where buoyancy effects due to the presence of a background density stratification have a leading-order influence on the flow, which corresponds to $Re_h \gg 1$ and $Fr_h \lesssim 1$. As Fr_h decreases below $O(1)$, horizontal motions tends to decouple into thin vertical layers with large horizontal extent, with the resulting vertical shearing being an important mechanism for generating turbulence (Lilly 1983). The resulting 'pancake' layers are predicted to evolve with vertical length scale U_h/N (Billant & Chomaz 2001), a behaviour that has been observed in experiments (e.g. Lin & Pao 1979; Spedding 1997), as well as in both forced and freely decaying DNS (e.g. Riley & de Bruyn Kops 2003; Brethouwer *et al.* 2007).

The SST regime exhibits anisotropy across a range of scales (Lang & Waite 2019), the largest of which is set by the vertical layered structure described above and whose existence is predicted by the value of Fr_h. Whether anisotropy persists at the smallest scales of motion (sometimes referred to as return to isotropy; Lumley & Newman 1977), thus affecting the way in which models for ε and χ depend on individual velocity and density derivatives, depends on the existence of an inertial range between these scales and the length scale of motion below which eddies evolve without being influenced by the stratification (Gargett, Osborn & Nasmyth 1984). For the velocity field, the breadth of the inertial range is characterised by an emergent Reynolds number, which for stratified flows is most commonly defined as the buoyancy Reynolds number

$$Re_b := \frac{\varepsilon}{\nu N^2}. \tag{1.2}$$

If $Re_b \ll 1$, scaling arguments and simulation results indicate that ε will be dominated by vertical shear (Riley, Metcalfe & Weissman 1981; Godoy-Diana, Chomaz & Billant 2004; de Bruyn Kops & Riley 2019). On the other hand, when $Re_b \gg 1$ and turbulence is locally almost isotropic, one can appeal to symmetry arguments to relate directly the

horizontal and vertical spatial derivatives of velocity and density, thus simplifying the expression for ε and χ (see e.g. Pope 2000). Several numerical studies quantify the degree of small-scale isotropy in SST as a function of Re_b (Hebert & de Bruyn Kops 2006; de Bruyn Kops 2015) from which we conclude that SST will be close to isotropic at the small scales if $Re_b \approx 50$ or larger. Importantly, there are many regions of the ocean in which it is estimated $Re_b < 50$ (e.g. Moum 1996; Jackson & Rehmann 2014; Scheifele *et al.* 2018), with potentially significant consequences for the accuracy of isotropic models for ε. When $Pr > 1$, density fluctuations are expected on smaller scales than those of velocity leading to the emergence of a viscous–convective subrange. Nonetheless, it may still be argued that the isotropic inertial range in the density field has the same high wavenumber cutoff as that of the velocity field (Batchelor 1959), and thus the breadth is again governed by Re_b. We note that technically even for $Re_b \gg 1$ the scalar derivatives cannot be exactly isotropic if there is a mean gradient (Warhaft 2000), although this detail will not be of practical importance for our purposes here. When only measurements of the density field are available, the buoyancy Reynolds number is sometimes replaced by the parameter $Pr^{-1}Cx$, where $Cx = |\nabla\rho|^2/(\partial\bar{\rho}/\partial z)^2$ is the Cox number for a flow with turbulent density fluctuations ρ about a background density profile $\bar{\rho}(z)$ (Dillon & Caldwell 1980).

Mean values of ε and χ can be accurately computed from single velocity and scalar derivatives if, by some method, the anisotropy in the velocity and scalar fields is known. This is the basis of the majority of existing models, e.g. estimating the dissipation rates by assuming isotropy. In practice, since Re_b itself depends on ε, it is not possible to diagnose precisely a turbulent regime given a limited subset of derivatives of velocity and density. Moreover, while the mean dissipation rates may be accurate based on assumptions of isotropy, the distribution of local values ε_0 and χ_0 (hereafter differentiated from appropriately averaged mean values ε and χ using a subscript 0) will not be. Using simulations of almost perfectly homogeneous isotropic turbulence, Almalkie & de Bruyn Kops (2012*b*) show that the probability density function (p.d.f.) of any of the velocity derivatives have nearly exponential left tails rather than the approximately log-normal tail assumed by Kolmogorov (1962) for the local dissipation rate, that is actually also widely observed in simulation data.

Motivated by the discussion above, in this work our primary aim will be to build highly general models for estimating local (ε_0, χ_0) and mean values (ε, χ) of the dissipation rates, that can make accurate predictions across a range of turbulent regimes described by different values of Re_b. We construct and train a probabilistic convolutional neural network (PCNN) model to compute local values of dissipation ε_0 and χ_0 within vertical fluid columns, motivated by available observational data collected by microstructure profilers. The architecture of the model is constructed based on the fundamental physical arguments that vertical gradients of velocity and density should be strongly correlated and of leading-order importance for determining local dissipation rates in stratified turbulence, crucially both locally and non-locally (for example, whether or not a particular region of fluid supports energetic turbulence is likely to depend at least on the local shear as well as some surrounding background density gradient) (Caulfield 2021). The probabilistic component is included based on the emerging importance of accurately predicting the tails of the distributions of values of small-scale mixing properties (Cael & Mashayek 2021; Couchman *et al.* 2021).

The data-driven models may be used as an effective tool revealing the fundamental limitations of theoretical models for local stratified turbulent flow properties derived based on global statistics. For this purpose, it will be important to compare the data-driven models with strict benchmarks whose functional form incorporates as many of the

currently known fluid dynamical constraints as possible. Therefore we also propose new empirically derived theoretical models for calculating ε_0 and χ_0 using the same inputs based on the knowledge that the local isotropy of the flow is primarily determined by the buoyancy Reynolds number Re_b, which here serve as a helpful baseline to compare with the deep learning model, but may also be considered practical substitutes for isotropic models in their own right. A comparison between the theoretical and PCNN models provides some interesting insights into the limitations of using mean quantities rather than local information for predicting mixing properties of stratified turbulent flows. Moreover, we analyse the structure of the optimised deep learning models to attempt to interpret which features give rise to improvements in accuracy over physics-based theoretical models.

To achieve our primary aim, the remainder of this paper is organised as follows. In § 2 we outline the key features of the DNS used throughout and describe how assumptions of isotropy may be used to construct models for ε and χ. We also present empirically determined theoretical models for ε and χ based on the value of a suitable proxy for the buoyancy Reynolds number Re_b, and introduce the probabilistic deep learning model to be evaluated against the theoretical models. Qualitative and quantitative comparisons are shown in § 3, and an analysis and interpretation of the deep learning model is carried out in § 4. We discuss some of the wider implications of the results and conclude in § 6.

2. Methods

2.1. *Simulations and theory*

Much of the ocean thermocline is believed to be in a 'strongly stratified turbulence' regime characterised by large Reynolds number and relatively small Froude number (Moum 1996; Brethouwer *et al.* 2007), defined by (1.1*a–c*), or in their 'turbulent' form by eliminating the horizontal length scale L_h in favour of a measured turbulent dissipation via the relation $\varepsilon = U_h^3/L_h$, as

$$Re_t = U_h^4/(\nu\varepsilon), \quad Fr_t = \varepsilon/(NU_h^2). \tag{2.1a,b}$$

For a flow with zero mean shear such as will be considered here, U_h is taken to be the root mean squared (r.m.s.) velocity and ε is volume averaged over the flow domain. In order to obtain a dataset of stratified turbulence that is broadly representative of a diverse and continuously evolving ocean environment, we appeal to DNS of decaying, strongly stratified turbulence with a large dynamic range accommodating motions on a wide range of spatial scales (de Bruyn Kops & Riley 2019). Simulations are carried out by solving the Navier–Stokes equations with the non-hydrostatic Boussinesq approximation, in the dimensionless form

$$\frac{\partial \boldsymbol{u}}{\partial t} + \boldsymbol{u}\cdot\boldsymbol{\nabla}\boldsymbol{u} = -\left(\frac{1}{Fr}\right)^2 \rho \boldsymbol{e}_z - \boldsymbol{\nabla} p + \frac{1}{Re}\nabla^2 \boldsymbol{u}, \tag{2.2}$$

$$\boldsymbol{\nabla}\cdot\boldsymbol{u} = 0, \tag{2.3}$$

$$\frac{\partial \rho}{\partial t} + \boldsymbol{u}\cdot\boldsymbol{\nabla}\rho - w = \frac{1}{RePr}\nabla^2\rho. \tag{2.4}$$

The dimensionless parameters Re, Pr and Fr are defined by

$$Re = \frac{U_0 L_0}{\nu}, \quad Fr = \frac{U_0}{NL_0}, \quad Pr = \frac{\nu}{\kappa}. \tag{2.5a–c}$$

Here, U_0 and L_0 are characteristic (horizontal) velocity and length scales of the flow in its initialised state, ν and κ are the momentum and density diffusivities and N is the (imposed and uniform) background buoyancy frequency. Density is non-dimensionalised using the scale $-L_0N^2\rho_a/g$, where g is the acceleration due to gravity and ρ_a is a reference density, whilst time is non-dimensionalised using the scale L_0/U_0. Note that ρ is defined as a departure from an imposed uniform background density gradient, so that the total dimensionless density ρ_t can be written (up to a constant reference density) as $\rho_t = \rho + z$.

Equations (2.2)–(2.4) are solved in a triply periodic domain using a pseudospectral method, with a third-order Adams–Bashforth method used to advance the equations in time and a 2/3 method of truncation for dealiasing fields. Simulations are initialised with the velocity fields in a state of homogeneous, isotropic turbulence. This is achieved by first performing unstratified simulations which are forced to match an empirical spectrum suggested by Pope (2000), using the method described in Almalkie & de Bruyn Kops (2012*b*). Once suitable conditions have been achieved, a gravitational field is imposed on the density stratification and forcing is switched off, leaving turbulence to decay freely. With the stratification applied, the flow evolves with a natural time scale given by the buoyancy period $T_B = 2\pi/N$. As discussed by de Bruyn Kops & Riley (2019), it is often instructive to observe the flow in terms of the number of buoyancy periods T after the stratification has been imposed.

The evolution of turbulence and its interaction with the background density stratification is dynamically rich and motions on a variety of length scales emerge which may be used to describe the instantaneous state of the flow. The largest-scale horizontal motions in the flow are described by the integral length scale L_h calculated here from the r.m.s. velocities using the method described in appendix E of Comte-Bellot & Corrsin (1971). This characterises the largest eddies which inject energy into turbulent motions. A turbulent cascade drives this energy down scale until it is dissipated as heat at the Kolmogorov scale L_K (or, for the density field, the Batchelor scale L_B). Two intermediate scales that arise due to the presence of the stratification are the buoyancy scale L_b and the Ozmidov scale L_O. The buoyancy scale is a vertical scale describing the height of the pancake layers that form, whilst the Ozmidov scale describes the size of the largest eddies which are unaffected by the stratification. These length scales are defined as follows:

$$L_K = (\nu^3/\varepsilon)^{1/4}, \quad L_B = L_K/Pr^{1/2}, \quad L_b = U_h/N, \quad L_O = (\varepsilon/N^3)^{1/2}. \qquad (2.6a\text{–}d)$$

De Bruyn Kops & Riley (2019) perform four simulations for various Fr and Re at $Pr = 1$. Here, we use data from a modified version of the simulation with largest Re which has $Pr = 7$ to be more representative of the ocean in regions where heat is the primary stratifying agent. Further details may be found in Riley, Couchman & de Bruyn Kops (2023). The Froude and Reynolds numbers for the simulation are $Fr = 1.1$ and $Re = 2480$. To obtain an appropriate rate of decay of turbulence, the horizontal domain size $L_x = L_y$ is chosen to initially accommodate roughly 84 integral length scales L_h, with the vertical extent $L_z = L_x/2$. To resolve motions adequately at the Batchelor scale L_B, this requires a maximum resolution of $N_x = N_y = 12\,880$, $N_z = N_x/2$. We take fully three-dimensional snapshots of the velocity and density fields (evenly sparsed by a factor of two in each coordinate direction for computational ease) at various time points $T = 0.5, 1, 2, 4, 6, 7.7$ during the flow evolution. This covers an extent of time over which the turbulence decays from being highly energetic and almost isotropic, to a near quasi-horizontal regime in which flow fields have the structure of thin horizontal layers, characteristic of stratified turbulence. The evolution of non-dimensional parameters Fr_h, Re_h, Fr_t, Re_t and Re_b describing the instantaneous state of the turbulence at each time point are given in table 1.

T	Re_h	Fr_h	Re_t	Fr_t	Re_b	L_K/Δ
0.5	2480	0.175	5880	0.118	81.2	1.1
1	1910	0.122	8200	0.0604	29.9	1.4
2	2020	0.0877	14660	0.0253	9.40	1.9
4	2390	0.0527	23850	0.0119	3.38	2.5
6	2390	0.0425	29030	0.0084	2.05	2.8
7.7	2430	0.0390	32270	0.0068	1.48	3.0

Table 1. Non-dimensional parameters for the simulation used at various numbers of buoyancy periods T following the introduction of the stratification. Note at $T = 0.5$ we have $Re_h = Re_0 = 2480$ and $Fr_h = Fr_0 = 0.175$. Here, $\Delta = L_x/(N_x/2)$ is the grid spacing of the snapshots, which are evenly sparsed by a factor of 2 in each coordinate direction from the DNS resolution.

2.2. *Dissipation rates and isotropic models*

The local (dimensionless) instantaneous rate of turbulent energy dissipation ε_0 is defined as

$$\varepsilon_0 = \frac{2}{Re} s_{ij} s_{ij}, \quad s_{ij} = \frac{1}{2}\left(\frac{\partial u_i}{\partial x_j} + \frac{\partial u_j}{\partial x_i}\right), \tag{2.7}$$

where the u_i represent turbulent velocity fluctuations. The corresponding local rate of potential energy dissipation χ_0 is defined as

$$\chi_0 = \frac{1}{RePr}\left(\frac{1}{Fr}\right)^2 \frac{\partial \rho}{\partial x_j}\frac{\partial \rho}{\partial x_j}. \tag{2.8}$$

As noted in the introduction, measuring the exact value of ε_0 and χ_0 requires that all spatial derivatives of the velocity and density fields be resolved, a task that is difficult even for laboratory flows, and certainly not possible at present in the context of oceanographic data. Thus it is common to make simplifying assumptions about the turbulence in order to proceed. If one assumes that turbulence is both homogeneous and isotropic, then averaging over some sufficient region, both expressions above can be written in terms of a single derivative. Microstructure profilers usually measure vertical derivatives, hence here we will consider the following isotropic models for ε_0 and χ_0:

$$\varepsilon_0^{iso} = \frac{15}{4Re} S^2; \quad S^2 := \left(\frac{\partial u}{\partial z}\right)^2 + \left(\frac{\partial v}{\partial z}\right)^2, \tag{2.9}$$

$$\chi_0^{iso} = \frac{3}{Re\,Pr}\left(\frac{1}{Fr}\right)^2 \left(\frac{\partial \rho}{\partial z}\right)^2. \tag{2.10}$$

Here, S^2 is the (squared) local vertical shear. As pointed out by Almalkie & de Bruyn Kops (2012*b*), these models are exact in the means (which here we take to be a spatial volume average denoted by angle brackets $\langle\cdot\rangle$) when turbulence is perfectly isotropic, but even in this idealised situation there may be significant differences in the frequency distributions of local values.

2.3. *An empirical model*

Equations (2.9) and (2.10) are only appropriate (strictly in the mean sense) provided that there exists an inertial range of scales above the Kolmogorov scale L_K (or equivalently for χ, the Batchelor scale L_B) within which the flow is close to isotropic. Noting that

we can write $Re_b = (L_O/L_K)^{4/3}$, whether or not such a range exists at small scales is primarily dependent on the value of the buoyancy Reynolds number, making this the most important parameter for determining the accuracy of the isotropic models above. Observational evidence supporting this hypothesis dates back to the measurements of Gargett *et al.* (1984), with many recent DNS confirming the agreement with the theory (see, e.g. de Bruyn Kops & Riley 2019; Lang & Waite 2019; Portwood, de Bruyn Kops & Caulfield 2019). Lang & Waite (2019) demonstrate that the primary effect of the Froude number Fr_h in this context is to control the larger-scale anisotropy. Therefore, even in a strongly stratified flow with $Fr_h \lesssim 1$, (2.9) and (2.10) are still expected to be accurate provided Re_b is sufficiently large.

When Re_b becomes small, buoyancy starts to dominate inertia at even the smallest vertical scales, prohibiting the formation of an inertial range. Consequently, the relative magnitudes of the velocity and density derivatives in (2.7) and (2.8) are expected to be substantially different from those predicted by isotropy, eventually being dominated by the vertical derivative terms in the limit $Re_b \ll 1$ as demonstrated (at least for ε) numerically and experimentally by, e.g. de Bruyn Kops & Riley (2019), Hebert & de Bruyn Kops (2006), Praud, Fincham & Sommeria (2005) and Fincham, Maxworthy & Spedding (1996). Therefore, as suggested by Hebert & de Bruyn Kops (2006), it is reasonable to suppose that the ratios ε/S^2 and $\chi/(\partial\rho/\partial z)^2$ should be a function of Re_b, giving a natural way of constructing models for ε and χ in stratified flows that take only vertical derivatives of velocity and density as inputs. The caveat of models constructed in this way is is that the additional required input Re_b is itself by definition a function of the desired output ε. To circumvent this issue, we appeal to a surrogate buoyancy Reynolds number

$$Re_b^S = -Fr^2 \frac{\langle S^2 \rangle}{\langle \partial\rho_t/\partial z \rangle}, \tag{2.11}$$

which at least varies monotonically with Re_b (and which we note is implicitly invoked via the isotropic assumption when working with observational data).

We wish to derive a local model for ε_0 and χ_0 that now depends on Re_b^S as well as S^2 and $\partial\rho/\partial z$. An important subtlety to note is the introduction of some ambiguity in defining a suitable surrogate buoyancy Reynolds number in the local picture due to how the (assumed) spatial averaging in (2.11) is interpreted. Such ambiguities can have appreciable effects on subsequently diagnosed turbulent statistics in stratified flows, as has been discussed by Arthur *et al.* (2017) and Lewin & Caulfield (2021). Because it describes anisotropy, which is inherently a non-local flow property, here we assume the 'true' Re_b^S is a bulk value averaged over the domain i.e. $Re_b^S = Fr^2\langle S^2 \rangle$ (since $\langle \partial\rho_t/\partial z \rangle = -1$ by construction). Of course, in the observational setting where measurements are limited, a representative bulk value may be computed by averaging a suitably large section of a vertical profile, over a scale at least as big as the Ozmidov scale L_O. However, this method may be ineffective when the flow is spatially separated into dynamically distinct regions as discussed by Portwood *et al.* (2016). This issue is circumvented by the data-driven model we present in § 2.4, which implicitly 'learns' the relevant non-local region of influence on local dissipation rates. With a suitably defined Re_b^S, we propose the following model:

$$\varepsilon_0^{emp} = \frac{f(Re_b^S)}{Re} S^2, \tag{2.12}$$

$$\chi_0^{emp} = \frac{g(Re_b^S)}{RePrFr^2} \left(\frac{\partial\rho}{\partial z}\right)^2, \tag{2.13}$$

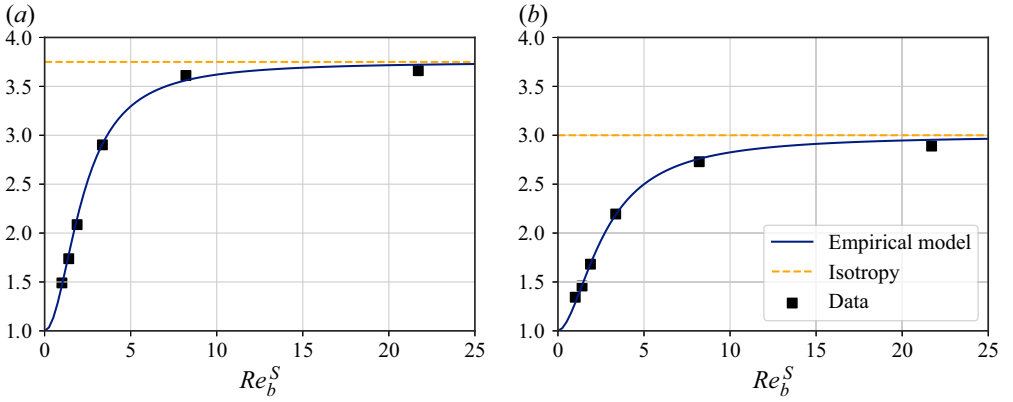

Figure 1. Values of the ratios (*a*) $Re\varepsilon/(\langle S^2\rangle)$ and (*b*) $Re\,Pr\,Fr^2\chi/(\langle\rho_z^2\rangle)$ for different values of the surrogate buoyancy Reynolds number Re_b^S. Here, Re_b^S is computed by interpreting the averaging in (2.11) as over the entire domain. The solid blue lines represent the empirical model functions (2.12) and (2.13), whilst the dashed lines represent the isotropic ratios from (2.9) and (2.10). Black markers represent the true values obtained from domain-averaged DNS quantities. The Jupyter notebook for producing the figure can be found https://www.cambridge.org/S0022112023006791/JFM-Notebooks/files/Fig1/fig1.ipynb.

where $f(Re_b^S)$ and $g(Re_b^S)$ are functions to be determined empirically, based on theoretical constraints. For $Re_b^S \gg 1$ the flow is locally isotropic and, in the mean sense, we should have $f \to 15/4$, $g \to 3$, as in (2.9) and (2.10). For $Re_b^S \ll 1$, horizontal diffusion becomes negligible and we therefore have $f \to 1$, $g \to 1$ (Riley *et al.* 1981; Godoy-Diana *et al.* 2004; de Bruyn Kops & Riley 2019). Data from the decaying turbulence simulation indicate a roughly linear transition from the viscously dominated $Re_b^S \ll 1$ regime to the isotropic $Re_b^S \gg 1$ regime, as shown in figure 1. Therefore, to match the required asymptotic behaviour and linear transition region, we propose the following models for the dimensionless functions f and g:

$$f(Re_b^S) = \tfrac{19}{8} + \tfrac{11}{8}\tanh(a\log Re_b^S - b), \tag{2.14}$$

$$g(Re_b^S) = 2 + \tanh(c\log Re_b^S - d). \tag{2.15}$$

Here, the constants b and d loosely represent the transition value between stratified turbulent and stratified viscous regimes, whilst a and c characterise the width of the transition region. These can be specified by a simple least-squares optimisation procedure that compares the functional approximations with the DNS data at the values of Re_b^S indicated in figure 1: it is found that empirical values of $a = 1, b = 0.8$ and $c = d = 0.9$ give an extremely close qualitative fit of the empirical function curves with the domain-averaged data, as can be seen in the figure. Note that in general $a \neq c$ and $b \neq d$ due to the difference in the smallest scales of motion caused by a non-unity Prandtl number $Pr = 7$, although in practice we see that these differences are relatively small (and largely insignificant).

There have been a limited number of attempts to model the influence of strong anisotropy on dissipation rates ε and χ. Weinstock (1981) proposes a modified model for ε in stratified turbulence that depends on r.m.s. vertical velocities $\langle w^2\rangle$ and the buoyancy frequency N. Fossum *et al.* (2013) instead suggest a model for ε in terms of χ, pointing out that χ itself may be replaced by vertical density derivatives via a suitable tuning coefficient. To our knowledge, the empirical models (2.12) and (2.13) constitute a first attempt to construct an explicit theoretical model for dissipation rates during the transition

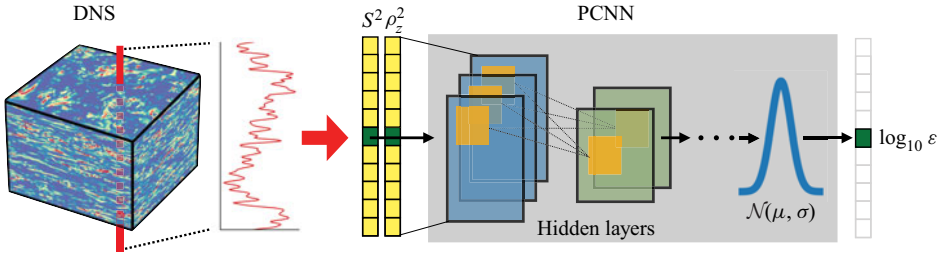

Figure 2. Schematic outlining the process of obtaining data from the DNS in vertical column format and the PCNN model architecture.

of such a flow from a near-isotropic to a buoyancy-dominated regime based on vertical derivatives of velocity and density only. Based on the theoretical scaling arguments discussed above, the functional forms of f and g are expected to remain independent of flow configuration, with the relevant asymptotic behaviour and linear transition having been observed in a number of previous forced and freely evolving DNS studies, e.g. Lang & Waite (2019), Brethouwer *et al.* (2007) and Hebert & de Bruyn Kops (2006). The transition value of Re_b^S and width of the transition region represented by the values of a, b, c and d also appear to be roughly consistent across studies, although a more detailed investigation would be required to quantitatively verify this. Here, (2.12) and (2.13) serve as useful comparative benchmarks for the data-driven model outlined below that are more strict than the isotropic models (2.9) and (2.10).

2.4. *Constructing a data-driven model*

2.4.1. *Model architecture*

Here, we construct a general model for computing local values of ε_0 and χ_0 from measurements of vertical derivatives of velocity and density, without explicitly appealing to arguments that rely on mean averaged quantities used for deriving the theoretical models above. We restrict ourselves to mimicking the oceanographic microstructure scenario where only vertical column measurements are available. To facilitate a comparison between this approach and the explicit theoretical models described above, we allow ε_0 to depend on local values of S^2 and χ_0 to depend on local values of $(\partial\rho/\partial z)^2$. We additionally allow both ε_0 and χ_0 to depend on the local value of the background (total) density gradient field $\partial\rho_t/\partial z$, which is suggested to be correlated with χ and ε in stratified turbulent flows in the sense that regions that are, or are close to being, statically unstable (positive background density gradient) are more likely to support more energetic turbulence (Portwood *et al.* 2016; Caulfield 2021). We anticipate that the precise dependencies on the inputs will be a function of the interaction of turbulence with buoyancy effects as would normally be characterised by the buoyancy Reynolds number, which we assume is unavailable as an input. We also might expect non-local correlations between the inputs with themselves and each other to be important. Finally, to capture the tails of the p.d.f.s of values of ε_0 and χ_0 accurately over a given region, it is beneficial to introduce a statistical component to the model whereby outputs are sampled from a distribution rather than predicted deterministically. This motivates the following log-normal models for local values of ε_0 and χ_0:

$$\log_{10}\varepsilon_0(z) \sim \mathcal{N}(\mu_\varepsilon, \sigma_\varepsilon); \tag{2.16}$$

$$\log_{10}\chi_0(z) \sim \mathcal{N}(\mu_\chi, \sigma_\chi), \tag{2.17}$$

where the means and variances of the distributions μ_a and σ_a are functions of the inputs, which we write generally as X_a and Y, for $a = \varepsilon, \chi$. We have $X_\varepsilon = S^2$ and $X_\chi = (\partial\rho/\partial z)^2$, whilst $Y = \partial\rho_t/\partial z$ is the same for both models. The functions μ_a and σ_a are to be determined, or 'learned' from the data

$$\mu_a = \mu_a(\{X_a(z+\delta)\}_{\delta\in[-\alpha,\alpha]}, \{Y(z+\delta)\}_{\delta\in[-\alpha,\alpha]}), \tag{2.18}$$

$$\sigma_a = \sigma_a(\{X_a(z+\delta)\}_{\delta\in[-\alpha,\alpha]}, \{Y_a(z+\delta)\}_{\delta\in[-\alpha,\alpha]}). \tag{2.19}$$

The interval $[-\alpha, \alpha]$, where α is a user-specified constant, represents the vertical height of the surrounding window of input values that the local output can depend on. We choose to make predictions of the logarithm of dissipation values for improved convergence during model training. Note that, because the μ_a and σ_a are functions of the inputs, the global distribution of outputs (i.e. over an entire vertical column) is not necessarily constrained itself to be log-normal, although in practice this is a classical theoretical prediction for isotropic turbulence (Kolmogorov 1962; Oboukhov 1962) and has been found to be accurate in many stratified decaying turbulent flows (de Bruyn Kops & Riley 2019).

The task is now to choose a functional form for μ_a and σ_a. We use a deep convolutional neural network which consists of several layers, each being a nonlinear function of outputs from the previous layer with j parameters β_j^L within each layer L (weights and biases) whose values are determined through an iterative optimisation procedure. Convolutional layers have a unique functional form which is highly suited to identifying structures or patterns in images, making them a natural choice for our model whose inputs are vertical columns of data with spatial structures over multiple different length scales. With the eventual outputs from the model being sampled from a distribution whose parameters are learnt by the network, we refer to the entire architecture as a PCNN, falling in a broader class of Bayesian deep learning frameworks known as mixture density networks.

We can write the inputs to the network in discrete form as $\{X_a(z+\delta)\}_{\delta\in[-\alpha,\alpha]} = \boldsymbol{X}_a = \{X_{a_1}, X_{a_2}, \ldots, X_{a_m}\}$, $\{Y(z+\delta)\}_{\delta\in[-\alpha,\alpha]} = \boldsymbol{Y} = \{Y_1, Y_2, \ldots, Y_m\}$, where the X_{ai} and Y_i represent m equispaced values sampled in the interval $z \in [-\alpha, \alpha]$. This is of course the natural representation for DNS where values of physical fields are discretely sampled at each grid point, and for oceanographic data where values are sampled at a particular frequency as the microstructure probe descends in the water column. Finally then, we write our data-driven neural network model as

$$\log_{10}\varepsilon_0^{NN}(z) \sim \mathrm{PCNN}_\varepsilon(\boldsymbol{X}_\varepsilon, \boldsymbol{Y}; \beta_j^L, \alpha), \tag{2.20}$$

$$\log_{10}\chi_0^{NN}(z) \sim \mathrm{PCNN}_\chi(\boldsymbol{X}_\chi, \boldsymbol{Y}; \gamma_j^L, \alpha), \tag{2.21}$$

where β_j^L and γ_j^L are trainable parameters. The PCNN used here comprises three fully connected convolutional layers with 32 filters and a kernel with a vertical height of 3 grid points, with a max-pooling layer between the second and third convolutional layers to reduce the dimensionality. The outputs from the convolutional layers are reshaped and fed into a dense layer which outputs values for μ_a and σ_a. For activation functions, we use the standard rectified linear unit, or ReLU, function in all layers. In total, there are roughly 60 000 training parameters to be optimised by fitting to the data.

2.4.2. *Dataset and training*

A schematic outlining the process of transforming the input columns from the DNS into local outputs of ε_0 is shown in figure 2. The model for χ_0 has an identical internal structure (highlighted in grey in the figure). To build the training dataset, we randomly sample

vertical columns of data from the three-dimensional field of the simulation described in table 1 at time steps $T = 0.5, 1, 2, 4, 7.7$, to give a total of approximately $n = 150\,000$ training samples. Note we intentionally withhold the time step $T = 6$ for testing. The chosen height 2α of input columns is a free parameter; for a fixed grid spacing this is determined by the number of grid points in the column m. Here, we take $m = 50$, which is largely justified by the sensitivity analysis detailed in § 4 demonstrating that outputs are relatively insensitive to inputs outside of this surrounding radius. A more thorough analysis can be found in the supplementary material available at https://doi.org/10.1017/jfm.2023.679. We then compute scaled values of local shear and vertical density gradients for each grid point within the columns

$$X_\varepsilon = \frac{1}{Re} S^2; \quad X_\chi = \frac{1}{RePr}\left(\frac{1}{Fr}\right)^2 \left(\frac{\partial \rho}{\partial z}\right)^2; \tag{2.22a,b}$$

$$Y = \frac{1}{\sqrt{RePr}}\left(\frac{1}{Fr}\right)\frac{\partial \rho_t}{\partial z}. \tag{2.23}$$

The resulting inputs are written as $\boldsymbol{X}_a^j = \{X_{a_1}^j, \ldots, X_{a_m}^j\}$ and $\boldsymbol{Y}^j = \{Y_1^j, \ldots, Y_m^j\}$, whilst the labels are denoted ε_0^j and χ_0^j. The labels are the exact values of the local dissipation defined in (2.7) evaluated at the midpoint of the input column, to be compared against model predictions. The prefactors of Re, Fr and Pr in front of X_a and Y are chosen based on dimensional considerations with (2.7) and (2.8), so that the model can be evaluated on data from simulations with different Re, Fr and Pr. Indeed, using dimensional inputs in a black-box model such as ours results in the undesirable situation of outputs whose physical dimensions are unknown. Note that, in our notation, X_{ai}^j denotes the value of the ith grid point from input $\boldsymbol{X}_a^j$, where the superscript $j \in \{1, \ldots, n\}$ indexes each individual data column.

The test set is a separate dataset from the same simulation used to assess qualitatively and quantitatively the performance of the network, which comprises two-dimensional (2-D) vertical snapshots of the flow at each time step obtained by sampling 250 horizontally adjacent columns, scaled in the same way as above. These columns can be fed through the network successively to obtain a model output of the entire 2-D snapshot. By design, the test set does not contain any columns of data previously sampled for the training set, and also contains data from the entirely unseen time step $T = 6$ as noted above.

The training and test data are normalised to improve convergence rates during model training (cf. 'whitening' in the machine learning literature, for instance LeCun *et al.* 2012)

$$\boldsymbol{X}_a^j \mapsto (\boldsymbol{X}_a^j - \bar{X})/\Sigma_{X_a}, \tag{2.24}$$

$$\boldsymbol{Y}^j \mapsto \boldsymbol{Y}^j/\Sigma_Y. \tag{2.25}$$

Here, $\bar{X}$ represents the mean of the inputs $\boldsymbol{X}_a$, and Σ_{X_a} and Σ_Y are similarly the standard deviations of the inputs $\boldsymbol{X}_a$ and $\boldsymbol{Y}$. These statistics are computed over the training set only as is standard practice. Note that we intentionally do not scale $\boldsymbol{Y}$ by its mean value. This is because the sign of the total vertical density derivative indicates whether a given grid point is in a statically stable density region ($\partial \rho_t/\partial z < 0$) or a statically unstable density region ($\partial \rho_t/\partial z > 0$). The static stability of a region of stratified turbulent flow has been previously linked to the intensity of turbulence and therefore ε; this is a dynamical feature we would like to be able to test for in our model.

Training is carried out by iteratively optimising a specified loss function $\mathcal{L}$ which measures the accuracy of model predictions over batches of training data that are successively and then repeatedly fed through the network. For the PCNN which predicts a distribution of outputs, we use a negative log-likelihood loss function which is a quantitative measure of the difference between the frequency distribution (or p.d.f.) of outputs and distribution of true labels over the batch

$$\mathcal{L} = \sum_{j \in \, batch} \log p^j. \tag{2.26}$$

Here, p^j is the value of the probability density function of the predicted distribution $\mathcal{N}(\mu^j, \sigma^j)$ of dissipation for column j evaluated at the true label ε^j. The Adam optimiser (Kingma & Ba 2014) with a learning rate of 0.005 is used to perform stochastic gradient descent. Good convergence was found after approximately 200 epochs (evaluations on each batch), which took around 5 minutes using TensorFlow on an NVIDIA Volta V100 GPU.

3. Results

3.1. *Model deployment*

Outputs ε_0 and χ_0 from the PCNN can be evaluated on the test data by either performing a single pass of inputs through the network to obtain a single output sample at each location in space, or by performing multiple passes of the same inputs through the network to generate an ensemble of outputs and taking the pointwise mean. As we will see, which of these two approaches is most powerful depends on the chosen metric used to evaluate model skill.

The isotropic models (2.9) and (2.10) and empirical models (2.12) and (2.13) are evaluated pointwise within each input column of data to obtain local predictions that may be compared with those of the PCNN. For the empirical models, the values of $\langle S^2 \rangle$ and $\langle \partial \rho_t / \partial z \rangle$ used in computing the surrogate buoyancy Reynolds number Re_b^S defined in (2.11) are computed by averaging over values within the input column corresponding to each point. Unlike the PCNN, both theoretical models are derived based on assumptions about the mean flow, but may be used still be used straightforwardly as described to make local predictions.

3.2. *Qualitative results*

A qualitative picture of outputs for ε_0 from the PCNN is shown in figure 3. The PCNN and empirical model (2.12) are evaluated on a 2-D snapshot from the test set at the time step $T = 6$ which is not seen during training. Single sample predictions from the PCNN are compared with the mean predictions from a 50-member ensemble. At $T = 6$, the surrogate buoyancy Reynolds number has dropped to $Re_b^S = 2.05$. Turbulence is still present, however, the flow is dominated by a vertical layered structure, with thin regions of higher dissipation in between 'quieter', more quiescent regions.

The empirical model (2.12) is designed to match the domain-averaged value of ε at each time step. In general the qualitative large-scale intermittency in the form of the vertical layers at low Re_b is well captured in terms of the shape and location of the dissipative layers as can be seen in panel (e), however, the quantitative magnitude of the local values of dissipation is clearly not well captured by this model as shown in panel (f) which shows

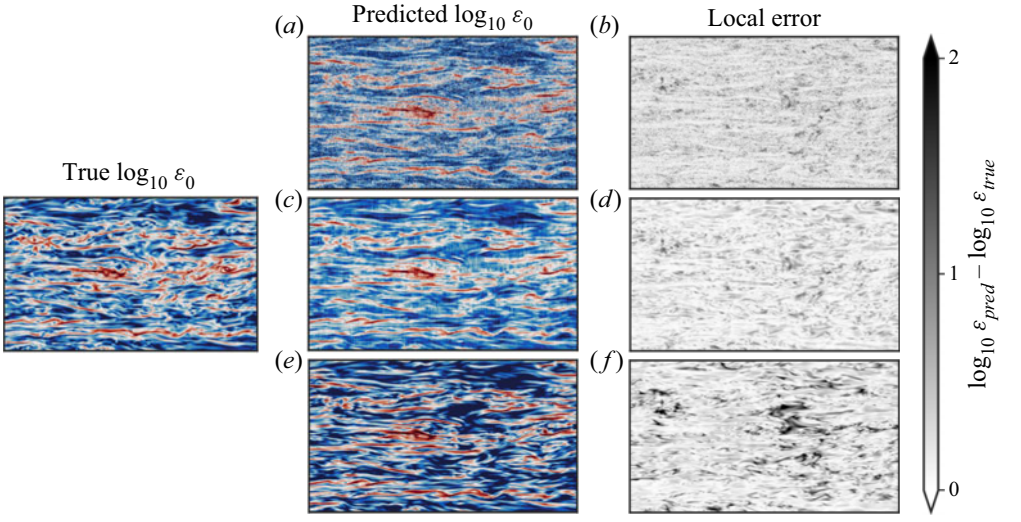

Figure 3. The left panel shows a 2-D vertical snapshot of kinetic energy dissipation ε_0 from the DNS at time $T = 6$, where red and blue colours represent higher and lower values of dissipation, respectively. The middle and right panels show values of ε predicted by the PCNN and empirical model (2.12) and their corresponding local errors. Panels (*a*) and (*b*) are predictions for a single sample of outputs from the PCNN; (*c*) and (*d*) are mean values calculated over an ensemble of 50 predictions; (*e*) and (*f*) are predictions from the empirical model (2.12). The Jupyter notebook for producing the figure can be found https://www.cambridge.org/S0022112023006791/JFM-Notebooks/files/Fig3/fig3.ipynb.

a strong spatial structure in the local prediction errors. In particular, the empirical model under-predicts values of dissipation in the quiescent blue regions by around 2 orders of magnitude. This is suggestive of the fact that the local dynamics within the dissipative layers and quiescent regions is distinct, a feature which has been proposed to be typical of stratified turbulence (Portwood *et al.* 2016; Caulfield 2021).

Both the single sample and ensemble mean PCNN models accurately reproduce the large-scale spatial structure of the flow. Moreover, they do not suffer from the same extreme local errors, and in this sense are preferable to the empirical model. It is interesting to compare between the two PCNN outputs in panels (*a*,*b*) and (*c*,*d*), respectively. The single sample PCNN outputs are more locally intermittent resulting in a grainy structure, although the large-scale features of the flow are clearly still well reproduced in both location and magnitude. As a result, the local errors are quite uniform in space. The mean ensemble PCNN outputs appear more washed out since the extreme high or low values of dissipation have been averaged out. This has one advantage that, at least through cursory examination, the local errors appear the smallest in general out of the three models shown.

Predictions on the same vertical slice for χ_0 are shown in figure 4. Due to the fact that the Prandtl number $Pr = 7$ so that density diffuses more slowly than momentum, structures are present at smaller scales than for ε_0. These smallest-scale structures are still well reproduced by the network, and just as before the large-scale anisotropy is accurately predicted. The local errors follow a similar pattern to the ε_0 case. The main noticeable difference between the PCNN for ε_0 and χ_0 is that the ensemble mean predictions for χ_0 are qualitatively superior in the sense that the extreme values appear better predicted.

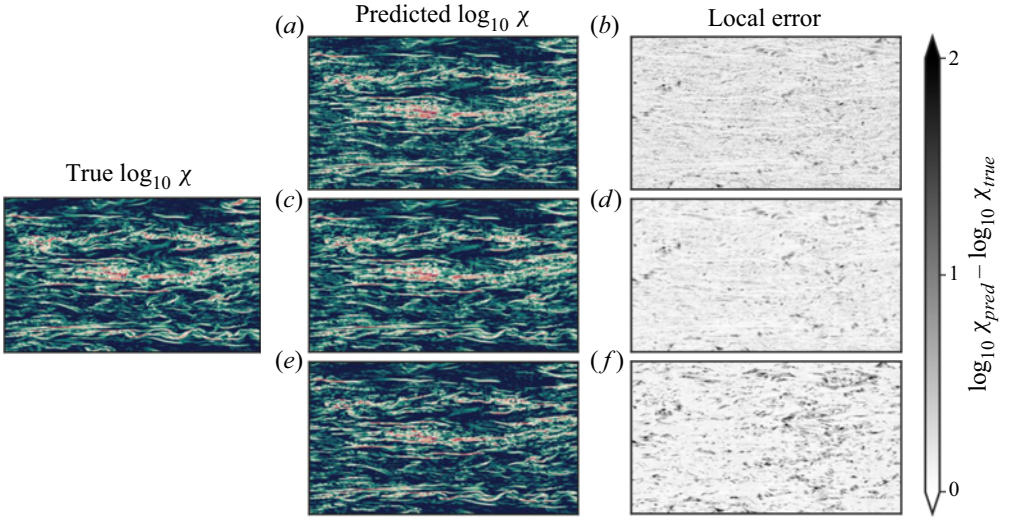

Figure 4. The same as figure 3 but this time showing predictions of χ_0. Red and green colours correspond to higher and lower values, respectively. The Jupyter notebook for producing the figure can be found https://www.cambridge.org/S0022112023006791/JFM-Notebooks/files/Fig4/fig4.ipynb.

3.3. *Quantitative results*

3.3.1. *Distributions*

We can form a more quantitative picture of the distribution of ε_0 by plotting the p.d.f.s of values at each time step. We note that each single sample of outputs from the PCNN produces an almost identical p.d.f., with the variation being predominantly in the spatial distribution of the values. Figure 5 shows the p.d.f.s for each model vs the DNS data at time steps $T = 1$ and $T = 7.7$, where the flow is close to isotropic and approaching viscous domination, respectively.

At $T = 1$, shown in figure 5(*a*), the isotropic model (2.9) and empirical model (2.12) coincide almost exactly as is to be expected since $Re_b \approx 30$ is sufficiently large for an inertial range to exist. However, even though they almost precisely match the DNS mean, there are still significant differences in the shape of the distribution, which is a well-documented feature in isotropic turbulence even without stratification (see, e.g. Hosokawa, Oide & Yamamoto 1996; Zhou & Antonia 2000; Cleve, Greiner & Sreenivasan 2003; Almalkie & de Bruyn Kops 2012*b*). A single sample of outputs from the PCNN matches the true DNS distribution almost exactly, with small deviations only at the extreme tails. This is particularly notable given that even models for the dissipation rate based on multiple velocity derivatives do not have the same shaped p.d.f. as that of dissipation rate itself (Almalkie & de Bruyn Kops 2012*b*). The effect of averaging over multiple ensemble members becomes clear looking at the distribution of predicted values, which is much narrower than the DNS distribution.

At $T = 7.7$, shown in figure 5(*b*), there is now a clear difference between the isotropic and empirical models which is to be expected at small Re_b. Even so, the fact that the empirical model is modified to match the mean does not change the shape of the distribution and the tails are still too wide compared with the DNS, which explains the differences in extreme values seen qualitatively in figure 3. Again, the single sample of PCNN outputs almost exactly matches the DNS distribution, whilst the presence of larger-scale layer structures in the flow means that the right tail of mean ensemble predictions is also a closer match to the DNS.

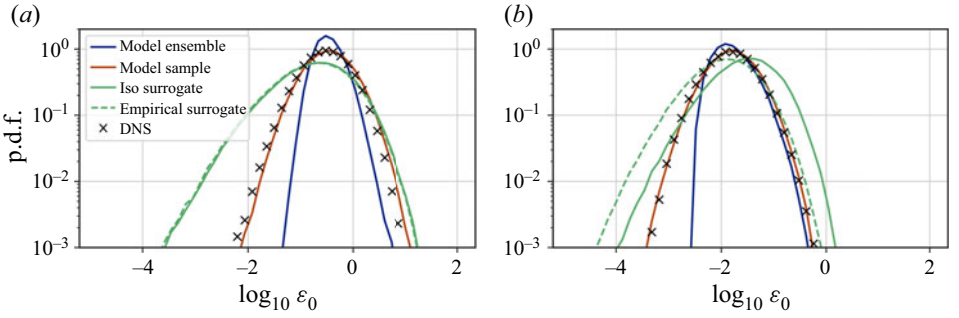

Figure 5. The p.d.f.s of $\log_{10} \varepsilon_0$ evaluated on a 2-D vertical slice from the test set at times (*a*) $T = 1$ and (*b*) $T = 7.7$. The black crosses represent the DNS data, whilst the coloured lines represent predictions from the PCNN (both a single sample and a mean over 50 ensemble members) and theoretical models (2.9) and (2.12) as indicated. Note the logarithmic *y*-axis. The Jupyter notebook for producing the figure can be found https://www.cambridge.org/S0022112023006791/JFM-Notebooks/files/Fig5/fig5.ipynb.

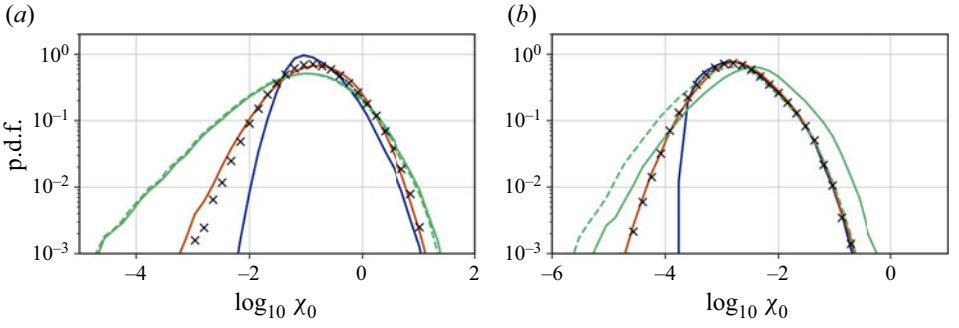

Figure 6. The same as figure 5 but for χ_0. The Jupyter notebook for producing the figure can be found https://www.cambridge.org/S0022112023006791/JFM-Notebooks/files/Fig6/fig6.ipynb. (*a*) $T = 1$ and (*b*) $T = 7.7$.

It is worth pointing out here that the PCNN is trained on data from all time steps simultaneously, and is given no explicit indication as to which time step a given input column has come from. Therefore, the fact that it is able to reproduce both the precise shape and location of the distribution of dissipation values as turbulence decays over time without being fed any explicit information about this decay is quite striking. In particular, it is more powerful than even the fitted empirical model in that it learns the transition of local flow statistics from a near-isotropic to a viscous-dominated regime whilst simultaneously accurately matching the evolution of the distribution of local structures as they evolve with time.

The equivalent results for χ_0 are shown in figure 6 and show a similar general pattern, although there are some notable differences. In general, the distributions of values for χ_0 are wider than they are for ε_0 which is to be expected for $Pr > 1$ due to the presence of smaller-scale spatial structures. The ensemble PCNN for χ_0 more closely reproduces the DNS distribution at $T = 1$ and $T = 7.7$ than the equivalent model for ε_0, particularly in the right tail. This matches the qualitative pictures in figure 4. We hypothesise that this could be due the presence of sharper interfaces in the χ_0 field which are better captured by the convolution operator in the PCNN. We also point out that even the single sample PCNN output does not quite capture the left-hand tail of the distribution at $T = 7.7$, although for practical purposes this is unlikely to be of major importance as the left tail is associated with very weak mixing.

3.3.2. *Mean relative error metrics*

We look at two quantitative measures of prediction error: the mean absolute error measured pointwise over a given vertical slice, and the mean absolute error of the column averaged values over the vertical slice, both normalised by the global mean

$$L_{pointwise} = \frac{1}{n}\sum_{j=1}^{n}\frac{\sum_{i=1}^{m}|\mu_j^i - y_{true_j}^i|}{\sum_{i=1}^{m}|y_{true_j}^i|}, \tag{3.1}$$

$$L_{columns} = \frac{1}{n}\sum_{j=1}^{n}\frac{\left|\sum_{i=1}^{m}(\mu_j^i - y_{true_j}^i)\right|}{\sum_{i=1}^{m}|y_{true_j}^i|}. \tag{3.2}$$

Here, μ_j^i are the means of the learnt local output distributions as described in § 2.4.1, n is the number of columns and m is the number of grid points within each column. Loosely speaking, these represent local and global measures of prediction error, respectively, where here 'global' refers to a column of data from the test set. An error of 1 then corresponds to a value that is, on average, 100 % of the column mean value.

Errors for ε_0 are shown in figure 7, plotted vs the corresponding (snapshot mean) Re_b for each time step. As expected, the isotropic model decreases in skill as Re_b decreases. The maximum mean relative error approaches twice the mean dissipation value for $Re_b \sim 1$. The PCNN models perform essentially as well as the isotropic model for high Re_b, and actually show a slight decrease in error as Re_b decreases, leading to significant improvements over the assumption of isotropy. The single sample PCNN predictions give similar errors to the empirical model (2.12), whilst the column mean predictions are actually slightly better than the predictions from the ensemble mean PCNN for most time steps, highlighting a potential advantage of accurately predicting the left and right tails of the distribution of values of ε_0. On the other hand, the ensemble mean predictions lead to a reasonable improvement for the pointwise values of ε_0. This is indicative of the difficulty of predicting small-scale turbulence intermittency: there are inevitable trade-offs to be made in accurately capturing the complete distribution of dissipation whilst also attempting to capture the spatial structure of this distribution completely.

Errors for χ_0 are shown in figure 8. The errors for the isotropic model (2.10) are less severe at low Re_b than the equivalent model for ε_0. This is likely due to $Pr > 1$, which gives rise to a wider range of scales between the Ozmidov scale L_O and the dissipation scale, which for χ is the Batchelor scale $L_B = L_K/Pr^{1/2}$. Therefore isotropy might be expected to be a reasonable assumption for χ at smaller values of Re_b than for ε. The performance of the PCNN models is once again at least as good as, or better than, the empirical models, most noticeably for the column mean predictions at small Re_b, where anisotropy is more marked.

4. Interpretation

We have seen that the data-driven PCNN models for ε_0 and χ_0 are at least as good as the proposed empirical models in making accurate predictions for the column mean, and

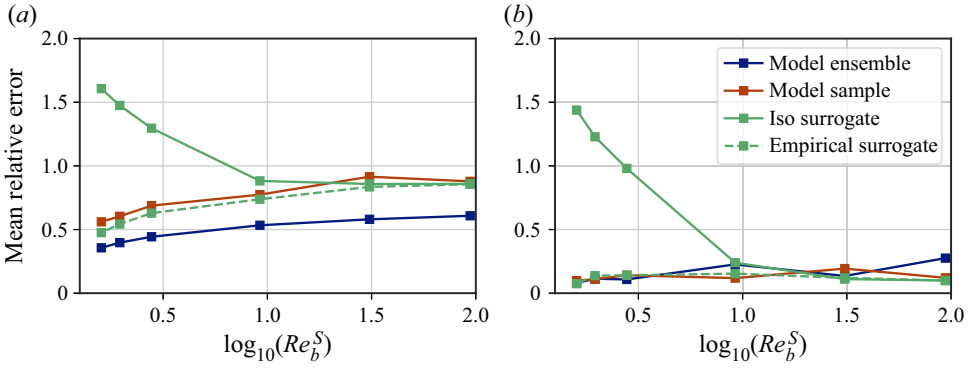

Figure 7. Mean relative error in ε_0 over the test set for the PCNN and theoretical models plotted against the logarithm of the buoyancy Reynolds number Gn. Panel (a) shows the mean error computed pointwise over each 2-D vertical snapshot, whilst (b) shows the mean error of column-averaged values of ε_0. The points from left to right are in order of decreasing time step (i.e. the left-most point is $T = 8$). The Jupyter notebook for producing the figure can be found https://www.cambridge.org/S0022112023006791/JFM-Notebooks/files/Fig7/fig7.ipynb.

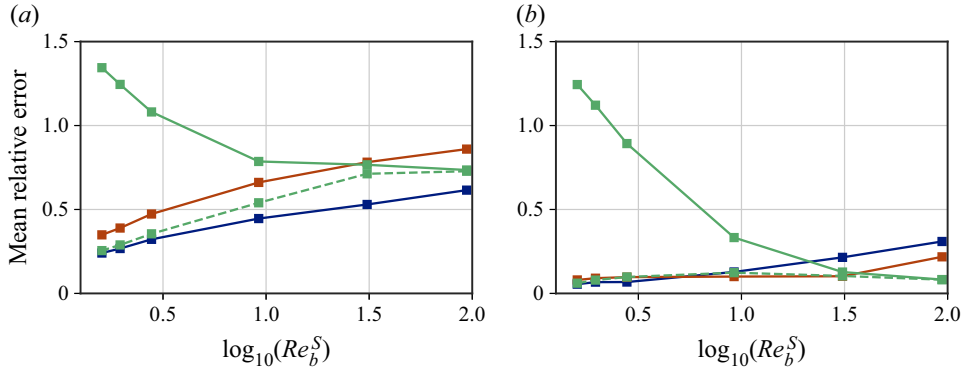

Figure 8. The same as figure 7 but for χ_0. Note the difference in y-axis limits between the two figures. The Jupyter notebook for producing the figure can be found https://www.cambridge.org/S0022112023006791/JFM-Notebooks/files/Fig8/fig8.ipynb. (a) Pointwise error and (b) column mean error.

they also offer an improvement in terms of the p.d.f.s of outputs and local pointwise prediction skill. Since the data-driven and theoretical models share common inputs, this motivates two immediate questions. Firstly, what are the functional similarities between these models? Secondly, what differences in the PCNN architecture allow it to outperform the theoretical models according to the performance metrics discussed above?

We can analyse the sensitivity of the predictions of ε_0 and χ_0 to the pointwise inputs to the network by exploring the gradients of the models at their predicted outputs. Calculating the gradients of the outputs with respect to the inputs at high numerical precision is made possible by the automatic differentiation capability of the Tensorflow framework which is used to perform gradient-based optimisation during training. This form of local gradient-based sensitivity analysis enables some comparison with the theoretical models (2.12) and (2.13). For complex image recognition tasks with deeper networks this method can be noisy and even unstable which has led to the development of methods such as layerwise relevance propagation as an improved method for handling output sensitivity (Montavon *et al.* 2017). Indeed, this method has been exploited in several geophysical settings (see for example Toms *et al.* 2020; Wang, Yuval & O'Gorman 2022). Here, we find it is sufficiently revealing for our purposes to perform a simple differential sensitivity

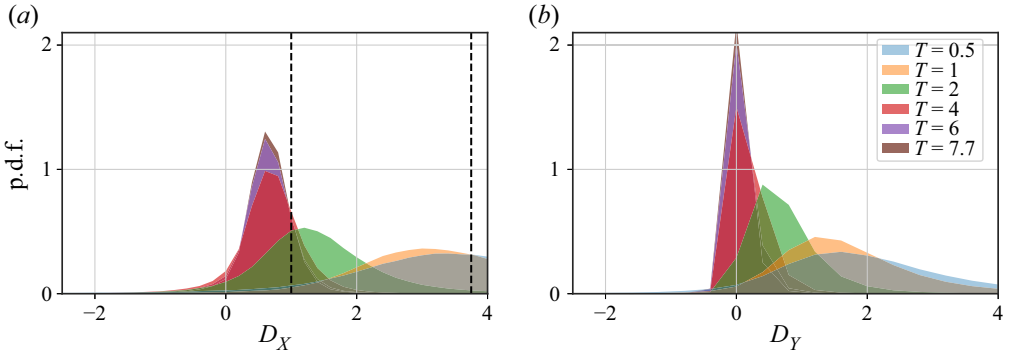

Figure 9. Distribution of sensitivities (*a*) $D^j_{X_\varepsilon}$ and (*b*) D^j_Y defined in (4.1) and (4.2) for outputs of ε_0^j at each time step in the test set as indicated by the colours, where here the inputs are $X_\varepsilon = (\partial u/\partial z)^2$ and $Y = \partial\rho_t/\partial z$. The dashed lines in panel (*a*) represent the isotropic and viscous-dominated values of 15/4 and 1, respectively. The Jupyter notebook for producing the figure can be found https://www.cambridge.org/S0022112023006791/JFM-Notebooks/files/Fig9/fig9.ipynb.

analysis of the network, as has been previously exploited in data-driven models for fluid dynamical systems (Gilpin *et al.* 2018; Portwood *et al.* 2021).

Since values of χ_0 and ε_0 predicted by the network depend non-locally on the inputs, we pose that a reasonable comparison with the (purely local) functional forms used in the theoretical isotropic and empirical models can be obtained by summing over the derivatives of the mean PCNN outputs with respect to each point within the input column, for each of the two input variables. That is, we look at the values of

$$D^j_{X_a} = \sum_i \frac{\partial \varepsilon_0^j}{\partial X^j_{ai}} = \ln(10)\varepsilon_0^j \sum_i \frac{\partial \mu^j}{\partial X^j_{ai}}, \tag{4.1}$$

$$D^j_{Y} = \sum_i \frac{\partial \varepsilon_0^j}{\partial Y^j_{i}} = \ln(10)\varepsilon_0^j \sum_i \frac{\partial \mu^j}{\partial Y^j_{i}}, \tag{4.2}$$

where we recall that the $\mu^j = \log_{10}\varepsilon_0^j$ are the means of the output distributions learnt by the network as described in § 2.4.1 and the chain rule has been used to facilitate a direct comparison of the PCNN with the isotropic and empirical models. For predictions of ε_0, note that the isotropic model (2.9) has by definition $D^j_{X_\varepsilon} = 15/4$, $D^j_Y = 0$, whilst the empirical model (2.12) has $D^j_{X_\varepsilon} = f(Re_b^S)$, $D^j_Y = 0$. The asymptotic limits are $D^j_{X_\varepsilon} = 15/4$ for $Re_b^S \gg 1$ and $D_{X_\varepsilon} = 1$ for $Re_b^S \ll 1$. For the PCNN, recall the inputs are $X_\varepsilon = S^2$ and $Y = \partial\rho_t/\partial z$.

The distributions of values of $D^j_{X_a}$ and D^j_Y evaluated on the test set for each time step are plotted in figure 9. Looking first at D_{X_ε} in figure 9(*a*), we see that the distribution of sensitivities moves to the left as T increases, matching what we expect physically. There is a reasonable spread in the distribution of values, indicating that the precise function mapping the inputs to the outputs varies locally. Looking at figure 9(*b*), we can see from the distribution of D^j_Y that there is a strong relative dependence on the background density gradient $Y = \partial\rho_t/\partial z$, particularly when the flow is more energetic at the earlier time steps. Clearly, the value of $\partial\rho_t/\partial z$ is important for determining the value of ε_0. We can see that, since in general $D^j_Y > 0$, positive values of $\partial\rho_t/\partial z$ are associated with larger values of

ε_0. Such points are statically unstable and so this directly supports the physical argument that these regions are important for determining where turbulence is most energetic, as presented by Portwood *et al.* (2016). Indeed, this feature of the PCNN makes it functionally distinct from the theoretical models and may explain why the centres of the distributions of $D^j_{X_\varepsilon}$ in panel (*a*) do not closely match the asymptotic limits for the first and last time steps $T = 0.5$ and $T = 7.7$.

We can probe this behaviour in more detail by looking at the non-local influence of the grid points in the column, i.e. looking at the local derivatives

$$d^j_{X_{ai}} = \frac{\partial \mu^j}{\partial X^j_{ai}}, \quad d^j_{Y_i} = \frac{\partial \mu^j}{\partial Y^j_i}. \tag{4.3a,b}$$

The theoretical models for ε_0 are entirely local i.e. $d^j_{X_{\varepsilon i}}$ is only non-zero at $i = m/2$, so that the prediction at each location depends only on the value of the inputs at that location. The PCNN is constructed to allow a non-local influence of the input columns on the outputs (which are the values of ε_0 at the centre of each input column). For each value of ε_0 in a row of data taken from the vertical test data snapshots, we plot the values of the local sensitivities $d^j_{X_{\varepsilon i}}$ and $d^j_{Y_i}$. This generates a heat map showing the sensitivities with respect to each grid point within the input columns, shown in figure 10. Since both inputs $X_\varepsilon = S^2$ and $Y = \partial \rho_T / \partial z$ have been established to be of similar importance for determining the value of ε_0, it is interesting to see the difference in their region of influence here. We see that ε_0 depends almost entirely locally on the shear inputs, but that there is a strong non-local influence of the background density gradient. This is entirely consistent with the hypothesis that the static stability of some suitably filtered background density field is important for determining characteristics of turbulence (Portwood *et al.* 2016; Caulfield 2021). Here, the 'filter' is represented by the convolution operator and has been learnt objectively and implicitly by the PCNN.

Turning to the predictions for χ_0, the isotropic model (2.10) has $D^j_{X_\chi} = 3$, $D^j_Y = 0$ and the empirical model (2.13) has $D^j_{X_\chi} = g(Re^S_b)$, $D^j_Y = 0$. The asymptotic limits are $D^j_{X_\chi} = 3$ for $Re^S_b \gg 1$ and $D^j_{X_\chi} = 1$ for $Re^S_b \ll 1$. Here, the PCNN has inputs $X_\chi = (\partial \rho / \partial z)^2$ and $Y = \partial \rho_t / \partial z$. The distributions of values of D_{X_a} and D_Y evaluated on the test set for each time step are plotted in figure 11. In general, the patterns in the distributions of D_{X_a} are similar to those for ε; however, there is a noticeable difference in that the centres of the distributions are now strongly aligned with the asymptotic limits for $T = 0.5$ and $T = 7.7$. This time, there is a less clear functional dependence on the total background density gradient $\partial \rho_t / \partial z$. This is indicative of the fact that indeed χ_0 and ε_0 are not always locally correlated, as discussed in more detail by Caulfield (2021) for example. Indeed, a comparison between figures 9(*b*) and 11(*b*) suggests that regions where they differ are functionally dependent on $\partial \rho_t / \partial z$ i.e. they are regions where local overturnings generate statically unstable regions with larger ε_0. These regions are often seen to be bounded above and below by interfaces of larger χ_0 leading to enhanced mixing efficiencies (Lewin & Caulfield 2021; VanDine, Pham & Sarkar 2021). Note that we do not produce an analogous plot corresponding to figure 10 since the values of the local sensitivities are much more noisy.

Finally, it is important to point out that the sensitivity analysis here by no means proves the existence of physical mechanisms underlying the functional relationships in the data, and indeed, using purely data-driven approaches to 'discover' new physics is still an open problem (Gilpin *et al.* 2018). However, we argue that our approach here of comparing

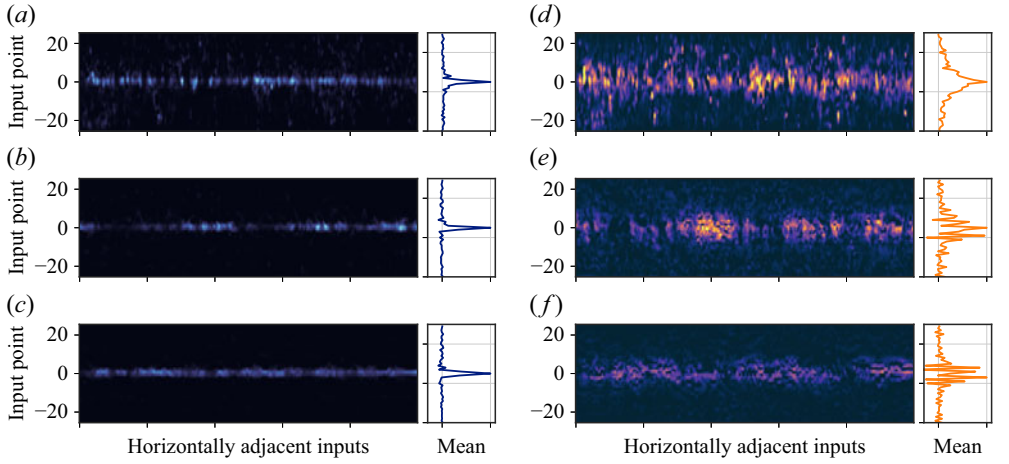

Figure 10. Sensitivities: $d^j_{X_{\varepsilon i}}$, shown in left column (*a–c*); and $d^j_{Y_i}$ shown in right column (*d–f*) for a row of predicted values of ε^j_0 within a vertical slice of test data to each of the grid points within the column of input data used to make the prediction. The corresponding time steps are: (*a*,*d*) $T = 0.5$; (*b*,*e*) $T = 4$; (*c*,*f*) $T = 8$. The PCNN makes predictions of the central value of dissipation within a column consisting of 50 grid points; in this way, the contour plots represent a heat map of the non-local influence of the surrounding grid points on the predicted central value for adjacent columns within the test set. A Gaussian filter has been applied to smooth out noise. The right-hand plot for each panel represents the average over all of the adjacent columns shown, normalised by the maximum value. The Jupyter notebook for producing the figure can be found https://www.cambridge.org/S0022112023006791/JFM-Notebooks/files/Fig10/fig10.ipynb.

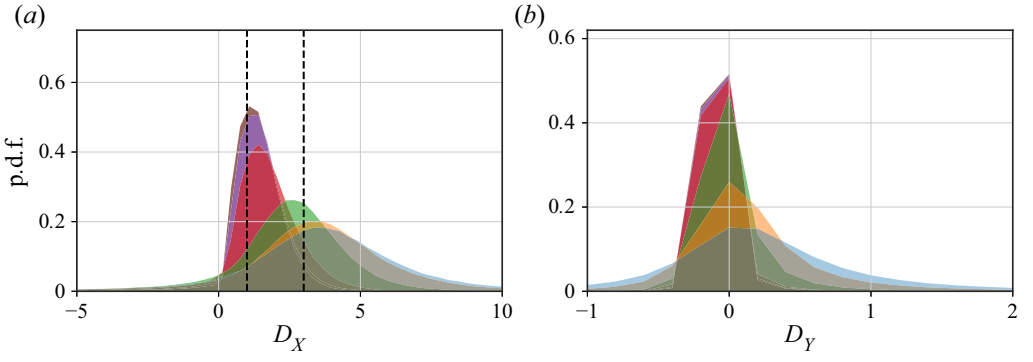

Figure 11. The same as figure 9 but for χ, where this time the inputs to the PCNN are $X_\chi = (\partial\rho/\partial z)^2$ and $Y = \partial\rho_t/\partial z$. The dashed lines in panel (*a*) represent the isotropic and layered viscous-dominated values of 3 and 1, respectively. Note the different axis limits between panels (*a*) and (*b*). The Jupyter notebook for producing the figure can be found https://www.cambridge.org/S0022112023006791/JFM-Notebooks/files/Fig11/fig11.ipynb.

a data-driven model with a theoretical model highlights some of the limitations of the construction of the latter, and lends support towards emerging hypotheses surrounding the relationship between the density and velocity fields in a stratified turbulent fluid (Portwood *et al.* 2016; Caulfield 2021).

5. Towards improved models for local turbulent statistics in stratified flows

The data-driven models proposed above target two fundamental limitations of existing models of small-scale dissipation rates in stratified turbulent flows. Firstly, flow fields at small scales may be strongly anisotropic due to the influence of buoyancy. Secondly,

models derived using averaged flow statistics are not guaranteed to be accurate below the averaging scale. As we have argued during the construction of the empirical models, the first limitation can in principle be addressed in theoretical models by making the reasonable assumption that the level of (small-scale) anisotropy is a function of the buoyancy Reynolds number, or in practice, some appropriate measurable surrogate such as Re_b^S. The decaying flow we have considered can be considered as an isolated turbulent patch within a larger-scale flow meaning Re_b^S is a reasonable proxy for the flow anisotropy, at least when averaged over a sufficiently large spatial region. Making accurate local predictions on scales smaller than this averaging region is still difficult, however, as is indicated by the distributions of local χ_0 and ε_0 predicted by the empirical models. The data-driven models demonstrate that this can be improved upon by incorporating a probabilistic component that more accurately captures small-scale intermittency.

Defining an appropriate Re_b^S may be considerably more complicated when the flow consists of distinct spatially separated regions between which the influence of buoyancy varies. In this situation, a value of Re_b^S calculated using an imprecisely diagnosed turbulent patch may result in the misrepresentation of smaller-scale local mixing events, as has been discussed in the context of mixing efficiency by Arthur *et al.* (2017) and Smyth & Moum (2000*b*). Portwood *et al.* (2016) introduce a robust patch identification method for such flows based on a thresholding procedure applied to the (suitably filtered) background density field. This motivated the architecture for the data-driven model, which was shown to detect an appropriate local region of influence of the background density field automatically without the need to specify a relevant filter width.

5.1. *Generalisation*

Motivated by the discussion above, we now evaluate the performance of the data-driven and empirical models on an entirely different flow configuration not seen during the training process. We use data from a statistically steady, forced simulation of stratified turbulence where the forcing is implemented using the scheme described in Almalkie & de Bruyn Kops (2012*a*) but the Prandtl number has been raised from $Pr = 1$ to $Pr = 7$ to match the training data here. Further details regarding the basic features of the $Pr = 1$ flow can be found in Portwood *et al.* (2016) and Couchman, de Bruyn Kops & Caulfield (2023). The bulk Froude, Reynolds and buoyancy Reynolds numbers are $Fr = 0.11$, $Re = 4100$, $Re_b = 50$, although, as noted by Portwood *et al.* (2016), the flow separates into dynamically distinct regions with significant variations in the corresponding flow parameters. This results in a wider spread of values of ε_0 and χ_0 than the decaying flow considered above.

As before, we evaluate the PCNN and empirical models on a 2-D vertical snapshot from the forced simulation. We are interested in whether empirical and data-driven models are capable of appropriately differentiating the local dynamics in the flow. For each grid cell, we notionally compute a surrounding 'patch' buoyancy Reynolds number $Re_b^{loc} = ReFr^2\langle\varepsilon_0\rangle$ by taking the average over a surrounding vertical region with extent given by the Taylor length scale computed from the bulk flow statistics as suggested by Portwood *et al.* (2016). By conditioning each cell according to Re_b^{loc} being greater or less than a nominal threshold value of 20, the p.d.f. of local ε_0 values can be separated about the mean into contributions from regions that are more strongly or more weakly influenced by buoyancy at small scales, demonstrated in figure 12(*a*). We note that this threshold value is consistent with the widely reported estimate of $O(10)$ at which motions start to become strongly anisotropic at small scales: for the flow we are considering, roughly half of the domain falls under this regime.

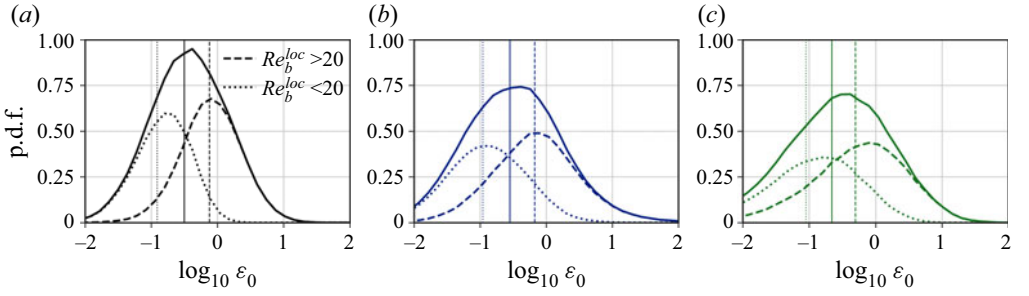

Figure 12. Solid curves show the p.d.f.s of $\log_{10}\varepsilon_0$ over a 2-D vertical snapshot of the forced simulation described in the text. Panel (*a*) shows true DNS values, (*b*) PCNN predictions and (*c*) empirical model predictions. Dashed and dotted curves represent the conditionally averaged p.d.f.s constructed from grid points that have Re_b^{loc} greater than or less than 20, which by construction sum together to give the total distribution. Vertical lines show the means of the respective distributions. The Jupyter notebook for producing the figure can be found https://www.cambridge.org/S0022112023006791/JFM-Notebooks/files/Fig12/fig12.ipynb.

Figure 12 demonstrates that the PCNN is capable of making accurate predictions on an unseen, substantially different flow configuration, at least with regards to the general shape and mean of the predicted p.d.f.s. This provides further evidence that the data-driven model has indeed learnt the general important underlying behaviour of a stratified turbulent system at moderate buoyancy Reynolds number. The performance compared with the empirical model is less qualitatively clear, although the data-driven model is certainly at least as accurate. More promisingly, when conditioned on Re_b^{loc}, the data-driven model is seen to differentiate between the corresponding flow regimes more accurately than the empirical model, with the latter producing a less distinctive split between the respective conditional p.d.f.s. In particular, the regions with smaller Re_b^{loc} are better captured by the data-driven model. This is again indicative of the local importance of buoyancy on small-scale motions that is captured by the data-driven model by using local vertical density gradient inputs, but not by the empirical model which is limited to the input of a larger-scale surrogate buoyancy Reynolds number Re_b^S.

5.2. *Limitations and improvements*

It is worth pointing out here that it is a well-known limitation of neural network-based model architectures that they do not handle out-of-distribution evaluation well, that is, when given inputs that fall outside the span of the training dataset. Lang & Waite (2019) argue that only one parameter, namely Re_b, is necessary for describing small-scale anisotropy in a stratified turbulent flow. Therefore, for the purposes of generalisation here, there is an implicit assumption that all stratified turbulent flows affected at leading order by buoyancy at small scales exhibit universal local similarity (specifically, at scales sufficiently below the buoyancy scale L_b) whose variation with Re_b is captured by the decaying DNS described in § 2.1 used to train the model. This is not an unreasonable assumption since the DNS covers the majority of the transition from near-isotropic turbulence to a viscous-dominated regime where buoyancy effects at small scales are important, but does mean that, for example, a network trained on only snapshots with $Re_b > 10$ would not be expected to make accurate predictions on snapshots that fall in the viscous-dominated regime. Importantly, however, this does not preclude the possibility that the network has learnt useful and relevant physical relationships in the data within the range it was trained on. Of course, present computational limitations restrict the range of buoyancy Reynolds numbers it is possible to achieve at low Froude number for such a

decaying simulation, so it is perhaps unsurprising that the data-driven model is unable to completely replicate the forced simulation data above given that a wider range of local Re_b are accessed in this flow configuration, providing better estimates for regions with $Re_b < 20$ which fall more centrally within the regimes encompassed by the training data. In principle, however, it is reasonable to expect a model trained on data spanning a sufficiently wide range of Re_b to be robust when evaluated on unseen data that can be described locally by a familiar dynamical regime.

6. Discussion and conclusions

Presently, no exact measurements of ε or χ exist in the ocean. Therefore data-driven models that are trained and/or evaluated on observational data are restricted to 'ground truth' values which are in fact estimates obtained from making significant simplifying assumptions (typically involving isotropy) about the turbulence. Such models may nonetheless be useful for making predictions on observations that do not accurately capture turbulence microstructure (such as, for example, Argo float data as reported by Waterhouse *et al.* 2014). Relevant here is the approach of Mashayek *et al.* (2022), who show that machine learning techniques can outperform classical fine structure methods for estimating diapycnal diffusivity which are used when microstructure measurements are not available. In this work, we adopt a different approach and instead look at the errors in the microstructure data themselves by using data from DNS of strongly stratified turbulence designed to reproduce conditions similar, or at least analogous to those found in the ocean interior. This has the advantage of allowing us to compare model predictions with exact values of turbulence statistics computed from the data, thus targeting directly the simplifying assumptions about turbulence used to obtain these statistics from microstructure measurements.

The primary aim of this work has been to demonstrate the efficacy of a novel deep learning algorithm for making localised predictions of dissipation of kinetic energy and scalar variance ε_0 and χ_0 from vertical column inputs of shear and density gradients. The resulting PCNN has an architecture constructed based on key physical considerations, including the evolving relationship between vertical shear and density gradients in the decaying stratified turbulent regime, the potential importance of statically unstable overturning regions indicated by positive density gradient and its non-local influence, and the statistical relevance of 'extreme' events corresponding to the tails of the input and output distributions. We also presented modified versions of isotropic models for ε_0 and χ_0 based on an empirical joining of two theoretically derived asymptotic regimes according to the value of the buoyancy Reynolds number $Re_b \ll 1$ or $Re_b \gg 1$. The PCNNs were trained on discrete snapshots from a dataset of initially isotropic decaying strongly stratified turbulence with zero mean shear, covering a range of values of Re_b. For applicability to other similar flows such as statistically stationary forced stratified turbulence, there is an implicit assumption that all stratified turbulent flows can be at least locally described as being in a regime described by some suitably spatially averaged Re_b according to the non-local influence of the background density gradient, as suggested by Portwood *et al.* (2016). The performance of the PCNN on unseen data from the DNS of forced stratified turbulence introduced in § 5 appears consistent with this hypothesis.

When tested on unseen data from the DNS, the PCNN models performed significantly better than commonly used isotropic models, and equally as well as the empirical models in terms of column-averaged value prediction. Moreover, these data-driven models had additional advantages over the empirical models in that they were able to make more accurate local predictions and much better capture the shape of the distribution of values

over multiple columns of data. The process of constructing the data-driven models alongside the physically motivated empirical models was useful for highlighting the limitations of theoretical turbulence models which rely on suitably averaged turbulence parameters, namely that they do not accurately model local distributions below the averaging scale and additionally may be biased when the averaging region spans dynamically distinct regions of the flow.

A differential sensitivity analysis of the network revealed some of the functional similarities and differences between the PCNN models and the theoretical models. Of particular note was the importance of non-local background density gradients for determining local values of ε_0 in a manner that is entirely consistent with the hypothesis that regions of static instability correspond to those of more energetic turbulence. The fact that this same correlation was not observed for χ_0 is indicative of the differences in local distributions between these two quantities which ultimately leads to enhanced mixing efficiency for 'extreme' mixing events, as discussed by Caulfield (2021) and identified in observational data by Couchman *et al.* (2021).

Indeed, the mixing efficiency of a stratified turbulent flow – defined here as $\eta = \chi/(\chi + \varepsilon)$ and interpreted as the percentage of turbulent energy expended in increasing the background potential energy of the flow – has received much of the focus in the fluid dynamics and oceanographic literature since it may be used to determine the diapycnal diffusivity κ_ρ which parameterises the turbulent flux of density across surfaces of constant density in the ocean, hence influencing the vertical redistribution of heat and other tracers (Ivey *et al.* 2008). Two relations due to Osborn (1980) and Osborn & Cox (1972) are commonly used to determine κ_ρ

$$\kappa_\rho^{Osborn} = \frac{\Gamma\varepsilon}{N^2}, \tag{6.1}$$

$$\kappa_\rho^{Cox} = \frac{\chi}{N^2}. \tag{6.2}$$

Here, $\Gamma = 1/(1-\eta)$ is known as the flux coefficient which for practical purposes is assumed to take the value of 0.2 but in reality is expected to vary with parameters of the flow such as (at least) Re_b, Fr_t and Pr, as reviewed by Gregg *et al.* (2018). Variations in Γ are usually reported to be within the range $0 < \Gamma < 0.5$ (although instantaneous values can be much larger, e.g. Mashayek, Caulfield & Peltier 2013). Our results here demonstrate that the relative magnitude of these variations compared with 0.2 are roughly the same as the uncertainties in ε that result from using assumptions of isotropy at moderate to low Re_b, and the latter therefore should be equally considered when inferring mixing rates from observations using Osborn's method (6.1). Since many parameterisations for Γ themselves depend on Re_b and hence ε (e.g. Bouffard & Boegman 2013), there is a potential for compound uncertainty in using (6.1). In particular, models for mixing efficiency exhibit similar uncertainties to those for dissipation investigated here due to ambiguities in how this parameter is defined, as discussed by Salehipour & Peltier (2015) and Arthur *et al.* (2017). This is likely to extend to other relevant parameters describing buoyancy effects at scales above the Ozmidov scale L_O such as an appropriately defined gradient Richardson number (Venayagamoorthy & Koseff 2016). As such, the Osborn–Cox method (6.2) is an appealing alternative because it avoids issues with the parameterisation of Γ; we point out that non-trivial errors may still be incurred from assuming isotropy.

In observational practice, values of χ and ε are obtained by either integrating over velocity and density gradient spectra over a suitable window or by fitting to an assumed universal spectrum in order to handle contaminating noise and/or a poorly resolved viscous

subrange when turbulence is energetic (see e.g. Bluteau, Jones & Ivey 2016; Bluteau *et al.* 2017). We have chosen here to focus on the relevance of the underlying physical assumptions about the turbulence revealed by our data-driven model, but it is obviously important to note that any practical implementation would require a detailed consideration of these observational limitations, in particular the response of the model to inputs that have been filtered to remove high wavenumbers. Nonetheless, our results indicate that measurements of ε and χ obtained assuming isotropy are likely to be overestimates when the 'true' flow $Re_b \lesssim 10$. From a practical perspective, the accuracy of the proposed empirical models (2.12) and (2.13) over a wide range of Re_b indicates that improvements over isotropy can be obtained by a (in principle) relatively simple modification to the relationship between ε and S^2, and χ and $(\partial\rho/\partial z)^2$, respectively, as a function of a suitably defined, and importantly, measurable, surrogate buoyancy Reynolds number Re_b^S. Note that it may also be important to consider the applicability of a universal spectral fitting function when turbulence is anisotropic at small scales, which may be the case even at moderate $Re_b \sim 10$.

From a fluid dynamics perspective, an important broader question that underpins the work here is: What is the optimal method for diagnosing representative turbulent statistics of a stratified fluid flow given sparse vertical column measurements? We have targeted a subset of this problem, showing that models for turbulent dissipation should depend at least on some measure of the influence of the buoyancy Reynolds number Re_b and some suitably averaged background density gradient $\partial\rho_t/\partial z$. There is evidence to suggest that other parameters not investigated here are likely to be of importance for modifying these dependencies. We argue that the turbulent Froude number Fr_t is not expected to be of major importance for models of (local) small-scale dissipation since it may be interpreted as a measure of larger-scale isotropy in the flow, as discussed by Lang & Waite (2019). The presence of a mean shear is likely to be of importance as has been discussed by Smyth & Moum (2000*a*) and Rehmann & Hwang (2005), although small-scale isotropy is still expected to be reproduced in the limit of large Re_b (Portwood *et al.* 2019). Indeed, recent work by Ivey, Bluteau & Jones (2018) and Young & Koseff (2022) has demonstrated the usefulness of a non-dimensional shear parameter for determining the value of the mixing coefficient Γ. As the results here indicate, suitably designed data-driven models, in combination with an intuition of the underlying dominant physical processes, may prove invaluable for both revealing and understanding the best way to model both the variation and uncertainties in the small-scale mixing properties of stratified turbulent flows.

Supplementary material. Supplementary material and Computational Notebook files are available at https://doi.org/10.1017/jfm.2023.679. Computational Notebooks can also be found online at https://cambridge.org/S0022112023006791/JFM-Notebooks.

Acknowledgements. The authors are grateful for the comments of three anonymous reviewers whose detailed comments helped improve the focus and overall quality of the manuscript. This work is based on the method presented in an earlier conference paper arXiv:2112.01113v1 by the same authors. The PCNN model described in this manuscript has been substantially extended and updated, and the results presented are entirely new.

Funding. This research used resources of the Oak Ridge Leadership Computing Facility at the Oak Ridge National Laboratory, which is supported by the Office of Science of the US Department of Energy under contract no. DE-AC05-00OR22725. S.F.L. is supported by an Engineering and Physical Sciences Research Council studentship from UKRI. S.deB.K. was supported under US Office of Naval Research grant number N00014-19-1-2152. The contributions from G.D.P. were performed under the auspices of the US Department of Energy by Lawrence Livermore National Laboratory under contract DE-AC52-07NA27344.

Declaration of interests. The authors report no conflict of interest.

Author ORCIDs.
Samuel F. Lewin https://orcid.org/0000-0002-2602-4751;
Stephen M. de Bruyn Kops https://orcid.org/0000-0002-7727-8786;
Colm-cille P. Caulfield https://orcid.org/0000-0002-3170-9480;
Gavin D. Portwood https://orcid.org/0000-0002-5685-4000.

References

ALMALKIE, S. & DE BRUYN KOPS, S.M. 2012*a* Kinetic energy dynamics in forced, homogeneous, and axisymmetric stably stratified turbulence. *J. Turbul.* **13**, N29.

ALMALKIE, S. & DE BRUYN KOPS, S.M. 2012*b* Energy dissipation rate surrogates in incompressible Navier–Stokes turbulence. *J. Fluid Mech.* **697**, 204–236.

ARTHUR, R.S., VENAYAGAMOORTHY, S.K., KOSEFF, J.R. & FRINGER, O.B. 2017 How we compute N matters to estimates of mixing in stratified flows. *J. Fluid Mech.* **831**, R2.

BARNES, E.A. & BARNES, R.J. 2021 Controlled abstention neural networks for identifying skillful predictions for regression problems. *J. Adv. Model. Earth Syst.* **13** (12), e2021MS002575.

BATCHELOR, G.K. 1959 Small-scale variation of convected quantities like temperature in turbulent fluid. Part 1. General discussion and the case of small conductivity. *J. Fluid Mech.* **5** (1), 113–133.

BEUCLER, T., PRITCHARD, M., RASP, S., OTT, J., BALDI, P. & GENTINE, P. 2021 Enforcing analytic constraints in neural networks emulating physical systems. *Phys. Rev. Lett.* **126** (9), 098302.

BILLANT, P. & CHOMAZ, J.-M. 2001 Self-similarity of strongly stratified inviscid flows. *Phys. Fluids* **13**, 1645–1651.

BLUTEAU, C.E., JONES, N.L. & IVEY, G.N. 2016 Estimating turbulent dissipation from microstructure shear measurements using maximum likelihood spectral fitting over the inertial and viscous subranges. *J. Atmos. Ocean. Technol.* **33** (4), 713–722.

BLUTEAU, C.E., LUECK, R.G., IVEY, G.N., JONES, N.L., BOOK, J.W. & RICE, A.E. 2017 Determining mixing rates from concurrent temperature and velocity measurements. *J. Atmos. Ocean. Technol.* **34** (10), 2283–2293.

BOLTON, T. & ZANNA, L. 2019 Applications of deep learning to ocean data inference and subgrid parametererization. *J. Adv. Model. Earth Syst.* **11** (1), 376–399.

BOUFFARD, D. & BOEGMAN, L. 2013 A diapycnal diffusivity model for stratified environmental flows. *Dyn. Atmos. Ocean* **61**, 14–34.

BRETHOUWER, G., BILLANT, P., LINDBORG, E. & CHOMAZ, J.-M. 2007 Scaling analysis and simulation of strongly stratified turbulent flows. *J. Fluid Mech.* **585**, 343–368.

BRUNTON, S.L., NOACK, B.R. & KOUMOUTSAKOS, P. 2020 Machine learning for fluid mechanics. *Annu. Rev. Fluid Mech.* **52**, 477–508.

DE BRUYN KOPS, S.M. 2015 Classical turbulence scaling and intermittency in stably stratified Boussinesq turbulence. *J. Fluid Mech.* **775**, 436–463.

DE BRUYN KOPS, S.M. & RILEY, J.J. 2019 The effects of stable stratification on the decay of initially isotropic homogeneous turbulence. *J. Fluid Mech.* **860**, 787–821.

CAEL, B.B. & MASHAYEK, A. 2021 Log-skew-normality of ocean turbulence. *Phys. Rev. Lett.* **126** (22), 224502.

CALLAHAM, J.L., KOCH, J.V., BRUNTON, B.W., KUTZ, J.N. & BRUNTON, S.L. 2021 Learning dominant physical processes with data-driven balance models. *Nat. Commun.* **12**, 1016.

CAULFIELD, C.P. 2021 Layering, instabilities and mixing in turbulent stratified flow. *Annu. Rev. Fluid Mech.* **53**, 113–145.

CLEVE, J., GREINER, M. & SREENIVASAN, K.R. 2003 On the effects of surrogacy of energy dissipation in determining the intermittency exponent in fully developed turbulence. *Europhys. Lett.* **61** (6), 756.

COMTE-BELLOT, G. & CORRSIN, S. 1971 Simple eulerian time correlation of full- and narrow-band velocity signals in grid-generated, 'isotropic' turbulence. *J. Fluid Mech.* **48** (2), 273–337.

COUCHMAN, M.M.P., DE BRUYN KOPS, S.M. & CAULFIELD, C.P. 2023 Mixing across stable density interfaces in forced stratified turbulence. *J. Fluid Mech.* **961**, A20.

COUCHMAN, M.M.P., WYNNE-CATTANACH, B., ALFORD, M.H., CAULFIELD, C.P., KERSWELL, R.R., MACKINNON, J.A. & VOET, G. 2021 Data-driven identification of turbulent oceanic mixing from observations of microstructure data. *Geophy. Res. Lett.* **48** (23), e2021GL094978.

DILLON, T.M. & CALDWELL, D.R. 1980 The Batchelor spectrum and dissipation in the upper ocean. *J. Geophys. Res.: Oceans* **85** (C4), 1910–1916.

FINCHAM, A.M., MAXWORTHY, T. & SPEDDING, G.R. 1996 Energy dissipation and vortex structure in freely decaying, stratified grid turbulence. *Dyn. Atmos. Ocean* **23** (1-4), 155–169.

FOSSUM, H.E., WINGSTEDT, E.M.M. & REIF, B.A.P. 2013 A model for the viscous dissipation rate in stably stratified, sheared turbulence. *Geophys. Res. Lett.* **40** (14), 3744–3749.
GARGETT, A.E., OSBORN, T.R. & NASMYTH, P.W. 1984 Local isotropy and the decay of turbulence in a stratified fluid. *J. Fluid Mech.* **144**, 231–280.
GILPIN, L.H, BAU, D., YUAN, B.Z, BAJWA, A., SPECTER, M. & KAGAL, L. 2018 Explaining explanations: an overview of interpretability of machine learning. In *2018 IEEE 5th International Conference on Data Science and Advanced Analytics (DSAA)*, pp. 80–89. IEEE.
GODOY-DIANA, R., CHOMAZ, J.-M. & BILLANT, P. 2004 Vertical length scale selection for pancake vortices in strongly stratified viscous fluids. *J. Fluid Mech.* **504**, 229–238.
GREGG, M.C., D'ASORO, E.A., RILEY, J.J. & KUNZE, E. 2018 Mixing efficiency in the ocean. *Annu. Rev. Mar. Sci.* **10**, 443–473.
GUILLAUMIN, A.P. & ZANNA, L. 2021 Stochastic-deep learning parameterization of ocean momentum forcing. *J. Adv. Model. Earth Syst.* **13**, e2021MS002534.
HEBERT, D.A. & DE BRUYN KOPS, S.M. 2006 Relationship between vertical shear rate and energy dissipation rate in stably stratified flows. *Geophys. Res. Lett.* **33** (6), L06602.
HOSOKAWA, I., OIDE, S. & YAMAMOTO, K. 1996 Isotropic turbulence: important differences between true dissipation rate and its one-dimensional surrogate. *Phys. Rev. Lett.* **77** (22), 4548.
IVEY, G.N., BLUTEAU, C.E. & JONES, N.L. 2018 Quantifying diapycnal mixing in an energetic ocean. *J. Geophys. Res. Oceans* **123**, 346–357.
IVEY, G.N., WINTERS, K.B. & KOSEFF, J.R. 2008 Density stratification, turbulence, but how much mixing? *Annu. Rev. Fluid Mech.* **40**, 169–184.
JACKSON, P.R. & REHMANN, C.R. 2014 Experiments on differential scalar mixing in turbulence in a sheared, stratified flow. *J. Phys. Oceanogr.* **44** (10), 2661–2680.
KINGMA, D.P. & BA, J. 2014 Adam: a method for stochastic optimization. arXiv:1412.6980.
KOLMOGOROV, A.N. 1962 A refinement of previous hypotheses concerning the local structure of turbulence in a viscous incompressible fluid at high Reynolds number. *J. Fluid Mech.* **13** (1), 82–85.
LANG, C.J. & WAITE, M.L. 2019 Scale-dependent anisotropy in forced stratified turbulence. *Phys. Rev. Fluids* **4**, 044801.
LECUN, Y.A., BOTTOU, L.O., GENEVIEVE, B. & MÜLLER, K.-R. 2012 Efficient backpropagation. In *Neural Networks: Tricks of the Trade*, pp. 9–48. Springer.
LEWIN, S.F. & CAULFIELD, C.P. 2021 The influence of far field stratification on shear-induced turbulent mixing. *J. Fluid Mech.* **927**, A20.
LILLY, D.K. 1983 Stratified turbulence and the mesoscale variability of the atmosphere. *J. Atmos. Sci.* **40**, 749–761.
LIN, J.-T. & PAO, Y.-H. 1979 Wakes in stratified fluids: a review. *Annu. Rev. Fluid Mech.* **11**, 317–338.
LING, J., KURZAWSKI, A. & TEMPLETON, J. 2016 Reynolds averaged turbulence modelling using deep neural networks with embedded invariance. *J. Fluid Mech.* **807**, 155–166.
LUMLEY, J.L. & NEWMAN, G.R. 1977 The return to isotropy of homogeneous turbulence. *J. Fluid Mech.* **82** (1), 161–178.
MASHAYEK, A., CAULFIELD, C.P. & PELTIER, W.R. 2013 Time-dependent, non-monotonic mixing in stratified turbulent shear flows: implications for oceanographic estimates of buoyancy flux. *J. Fluid Mech.* **736**, 570–593.
MASHAYEK, A., REYNARD, N., ZHAI, F., SRINIVASAN, K., JELLEY, A., NAVEIRA GARABATO, A. & CAULFIELD, C.P. 2022 Deep ocean learning of small scale turbulence. *Geophys. Res. Lett.* **49** (15), e2022GL098039.
MAULIK, R., FUKAMI, K., RAMACHANDRA, M., FUKAGATA, K. & TAIRA, K. 2020 Probabilistic neural networks for fluid flow surrogate modeling and data recovery. *Phys. Rev. Fluids* **5** (10), 104401.
MAULIK, R., SAN, O., RASHEED, A. & VEDULA, P. 2019 Subgrid modelling for two-dimensional turbulence using neural networks. *J. Fluid Mech.* **858**, 122–144.
MONTAVON, G., LAPUSCHKIN, S., BINDER, A., SAMEK, W. & MÜLLER, K.-R. 2017 Explaining nonlinear classification decisions with deep Taylor decomposition. *Pattern Recognit.* **65**, 211–222.
MOUM, J.N. 1996 Energy-containing scales of turbulence in the ocean thermocline. *J. Geophys. Res.: Oceans* **101** (C6), 14095–14109.
OBOUKHOV, A.M. 1962 Some specific features of atmospheric tubulence. *J. Fluid Mech.* **13** (1), 77–81.
OSBORN, T.R. 1980 Estimates of the local rate of vertical diffusion from dissipation measurements. *J. Phys. Oceanogr.* **10**, 83–89.
OSBORN, T.R. & COX, C.S. 1972 Oceanic fine structure. *Geophys. Fluid Dyn.* **3** (4), 321–345.
POPE, S.B. 2000 *Turbulent Flows*. Cambridge University Press.

PORTWOOD, G.D., DE BRUYN KOPS, S.M. & CAULFIELD, C.P. 2019 Asymptotic dynamics of high dynamic range stratified turbulence. *Phys. Rev. Lett.* **122** (19), 194504.

PORTWOOD, G.D., DE BRUYN KOPS, S.M., TAYLOR, J.R., SALEHIPOUR, H. & CAULFIELD, C.P. 2016 Robust identification of dynamically distinct regions in stratified turbulence. *J. Fluid Mech.* **807**, R2.

PORTWOOD, G.D., NADIGA, B.T., SAENZ, J.A. & LIVESCU, D. 2021 Interpreting neural network models of residual scalar flux. *J. Fluid Mech.* **907**, A23.

PRAUD, O., FINCHAM, A.M. & SOMMERIA, J. 2005 Decaying grid turbulence in a strongly stratified fluid. *J. Fluid Mech.* **522**, 1–33.

RASP, S., PRITCHARD, M.S. & GENTINE, P. 2018 Deep learning to represent subgrid processes in climate models. *Proc. Natl Acad. Sci. USA* **115** (39), 9684–9689.

REHMANN, C.R. & HWANG, J.H. 2005 Small-scale structure of strongly stratified turbulence. *J. Phys. Oceanogr.* **35** (2), 151–164.

RILEY, J.J. & DE BRUYN KOPS, S.M. 2003 Dynamics of turbulence strongly influenced by buoyancy. *Phys. Fluids* **15** (7), 2047–2059.

RILEY, J.J., COUCHMAN, M.P.P. & DE BRUYN KOPS, S.M. 2023 The effect of Prandtl number on decaying stratified turbulence. *J. Turbul.* (submitted).

RILEY, J.J. & LINDBORG, E. 2008 Stratified turbulence: a possible interpretation of some geophysical turbulence measurements. *J. Atmos. Sci.* **65** (7), 2416–2424.

RILEY, J.J., METCALFE, R.W. & WEISSMAN, M.A. 1981 Direct numerical simulations of homogeneous turbulence in density-stratified fluids. In *AIP Conference Proceedings*, vol. 76, pp. 79–112. American Institute of Physics.

SALEHIPOUR, H. & PELTIER, W.R. 2015 Diapycnal diffusivity, turbulent Prandtl number and mixing effiency in Boussinesq stratified turbulence. *J. Fluid Mech.* **775**, 464–500.

SALEHIPOUR, H. & PELTIER, W.R. 2019 Deep learning of mixing by two 'atoms' of stratified turbulence. *J. Fluid Mech.* **861**, R4.

SCHEIFELE, B., WATERMAN, S., MERCKELBACH, L. & CARPENTER, J.R. 2018 Measuring the dissipation rate of turbulent kinetic energy in strongly stratified, low-energy environments: a case study from the arctic ocean. *J. Geophys. Res.: Oceans* **123** (8), 5459–5480.

SMYTH, W.D. & MOUM, J.N. 2000*a* Length scales of turbulence in stably stratified mixing layers. *Phys. Fluids* **12**, 1327–1342.

SMYTH, W.D. & MOUM, J.N. 2000*b* Anisotropy of turbulence in stably stratified mixing layers. *Phys. Fluids* **12** (6), 1343–1362.

SPEDDING, G.R. 1997 The evolution of initially turbulent bluff-body wakes at high internal Froude number. *J. Fluid Mech.* **337**, 283–301.

SUBEL, A., CHATTOPADHYAY, A., GUAN, Y. & HASSANZADEH, P. 2021 Data-driven subgrid-scale modeling of forced burgers turbulence using deep learning with generalization to higher Reynolds numbers via transfer learning. *Phys. Fluids* **33** (3), 031702.

TALLEY, L.D., *et al.* 2016 Changes in ocean heat, carbon content, and ventilation: a review of the first decade of GO-SHIP global repeat hydrography. *Annu. Rev. Mar. Sci.* **8**, 185–215.

TOMS, B.A., BARNES, E.A. & EBERT-UPHOFF, I. 2020 Physically interpretable neural networks for the geosciences: applications to earth system variability. *J. Adv. Model. Earth Syst.* **12** (9), e2019MS002002.

VANDINE, A., PHAM, H.T. & SARKAR, S. 2021 Turbulent shear layers in a uniformly stratified background: DNS at high Reynolds number. *J. Fluid Mech.* **916**, A42.

VENAYAGAMOORTHY, S.K. & KOSEFF, J.R. 2016 On the flux Richardson number in stably stratified turbulence. *J. Fluid Mech.* **798**, R1.

WANG, P., YUVAL, J. & O'GORMAN, P.A. 2022 Non-local parameterization of atmospheric subgrid processes with neural networks. *J. Adv. Model. Earth Syst.* **14** (10), e2022MS002984.

WARHAFT, Z. 2000 Passive scalar in turbulent flows. *Annu. Rev. Fluid Mech.* **32**, 203–240.

WATERHOUSE, A.F., *et al.* 2014 Global patterns of diapycnal mixing from measurements of the turbulent dissipation rate. *J. Phys. Oceanogr.* **44** (7), 1854–1872.

WEINSTOCK, J. 1981 Energy dissipation rates of turbulence in the stable free atmosphere. *J. Atmos. Sci.* **38** (4), 880–883.

YOUNG, R.Y. & KOSEFF, J.R. 2022 Revised mixing coefficient scaling for sheared stably stratified turbulence. *J. Fluid Mech.* **952**, A18.

ZANNA, L. & BOLTON, T. 2020 Data-driven equation discovery of ocean mesoscale closures. *Geophys. Res. Lett.* **47** (17), e2020GL088376.

ZHOU, T. & ANTONIA, R.A. 2000 Approximations for turbulent energy and temperature variance dissipation rates in grid turbulence. *Phys. Fluids* **12** (2), 335–344.